J. Fluid Mech. (2011), *vol.* 676, *pp.* 396–431. © Cambridge University Press 2011
doi:10.1017/jfm.2011.57

Shock-wave surfing

S. J. LAURENCE[1]† AND R. DEITERDING[2]

[1]Institute of Aerodynamics and Flow Technology, Spacecraft Section, German Aerospace Center, Bunsenstraße 10, 37073 Göttingen, Germany

[2]Oak Ridge National Laboratory, PO Box 2008 MS6367, Oak Ridge, TN 37831, USA

(Received 8 July 2010; revised 29 January 2011; accepted 1 February 2011; first published online 6 April 2011)

A phenomenon referred to as 'shock-wave surfing', in which a body moves in such a way as to follow the shock wave generated by another upstream body, is investigated numerically and analytically. During the surfing process, the downstream body can accumulate a significantly higher lateral velocity than would otherwise be possible. The surfing effect is first investigated for interactions between a sphere and a planar oblique shock. Numerical simulations are performed and a simple analytical model is developed to determine the forces acting on the sphere. A phase-plane description is employed to elucidate features of the system dynamics. The analytical model is then generalised to the more complex situation of aerodynamic interactions between two spheres, and, through comparisons with further computations, is shown to adequately predict the final separation velocity of the surfing sphere in initially touching configurations. Both numerical simulations and a theoretical analysis indicate a strong influence of the sphere radius ratio on the separation process and predict a critical radius ratio that delineates entrainment of the smaller body within the flow region bounded by the larger body's shock from expulsion. Furthermore, it is shown that an earlier scaling law does not accurately describe the separation behaviour. The surfing effect has important implications for meteoroid fragmentation: in particular, a large fraction of the variation in the separation velocity deduced by previous authors from an analysis of terrestrial crater fields can be explained by a combination of surfing and a modest rotation rate of the parent body.

Key words: flow–structure interactions, high-speed flow, shock waves

1. Introduction

The problem of aerodynamic interactions between bodies travelling at hypersonic speeds is an interesting topic of study in its own right, but is also important to our understanding of such phenomena as the fragmentation of meteoritic bodies in the atmospheres of Earth and other planets. The separation behaviour of fragments immediately following atmospheric disruption is determined to a large extent by aerodynamic effects (Passey & Melosh 1980), and this in turn can determine, for instance, the arrangement of craters in the strewn field formed by fragments that survive the atmospheric transit, or the damage produced at the planetary surface by bodies that explode in the atmosphere (Hills & Goda 1993). For bodies that are disrupted into a limited number of distinct fragments, rather than heavily fragmented into a liquid- or swarm-like mass (Chyba, Thomas & Zahnle 1993;

† Email address for correspondence: stuart.laurence@dlr.de

https://doi.org/10.1017/jfm.2011.57 Published online by Cambridge University Press

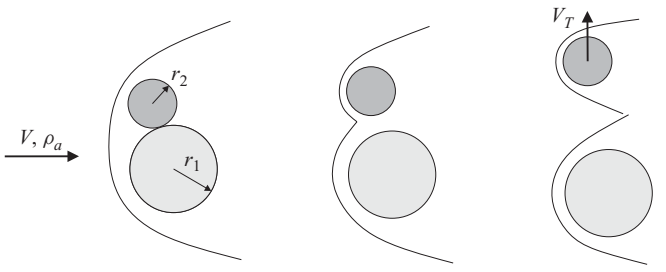


FIGURE 1. The lateral separation model for two unequally sized bodies proposed by Passey & Melosh (1980).

Svetsov, Nemtchinov & Teterev 1995), it is necessary to consider the shock interactions between fragments to gain an accurate picture of the separation process.

The first to consider in detail the separation of distinct meteoroid fragments were Passey & Melosh (1980), who assumed a purely lateral separation due to bow-shock interactions between two fragments of radii $r_1 \geqslant r_2$, as shown in figure 1. The smaller body is predicted to develop a final separation velocity, V_T, of

$$V_T = \sqrt{C \frac{r_1}{r_2} \frac{\rho_a}{\rho_m}} V, \tag{1.1}$$

where V is the velocity of the meteoroid through the atmosphere, ρ_a and ρ_m are the densities of the atmosphere and the meteoroid, respectively, C is a constant that, through examining various terrestrial crater fields, was determined by Passey & Melosh to take a value between 0.03 and 2.25. As much of the subsequent work on the topic has involved the modelling of equally sized fragments, (1.1) is often rewritten as

$$V_T = \sqrt{C \frac{\rho_a}{\rho_m}} V. \tag{1.2}$$

Here, we do so in anticipation that (1.1) does not provide an accurate representation of the scaling of V_T with r_2/r_1.

Employing numerical simulations to investigate the symmetrical separation of two identical fragments, Artem'eva & Shuvalov (1996) determined a value of C in (1.2) of approximately 0.2; their results also showed that the lateral force acting on a trailing body within the flow region downstream of the bow-shock created by a leading body is attractive. This confirmed the collimation effect observed experimentally by Schultz & Sugita (1994), in which individual particles in a debris cloud were seen to 'surf' over the cloud shock front and become entrained within the shock layer. Subsequent numerical simulations of up to 27 identical fragments (Artemieva & Shuvalov 2001) indicated a value of C of approximately unity. Models based on these findings have been used in simulating the break-up of meteoritic bodies in the atmosphere and to draw conclusions, for example, regarding the rate of arrival of small asteroids at the Earth's surface (Bland & Artemieva 2003, 2006; Artemieva & Pierazzo 2009). Further work involving the modelling of stationary bodies (Laurence, Deiterding & Hornung 2007; Barri 2009) has contributed to our understanding of the aerodynamic interactions between fragments of different sizes; however, the effect of

https://doi.org/10.1017/jfm.2011.57 Published online by Cambridge University Press

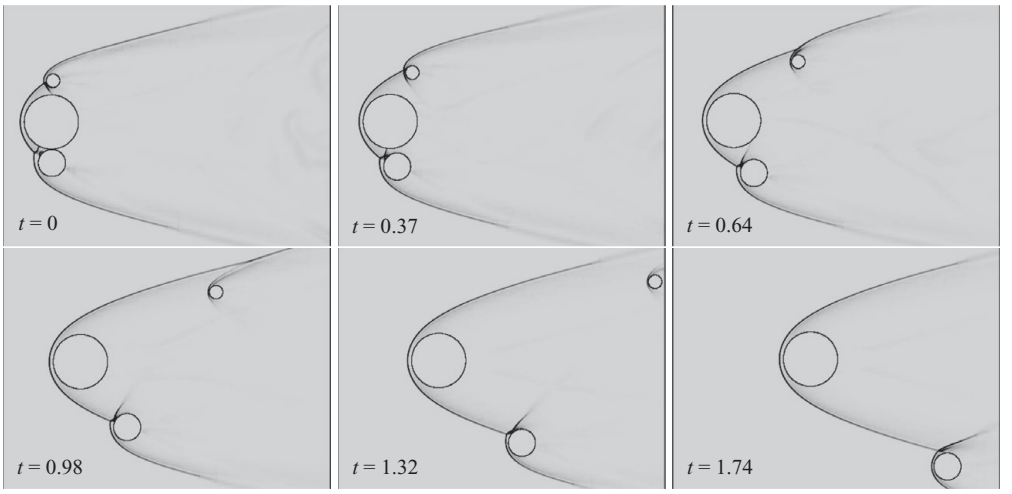


FIGURE 2. 'Shock-wave surfing', in which a smaller body rides downstream on the bow-shock created by a larger body. As a result, the smaller body can either be entrained within the flow region downstream of the main bow-shock (e.g. upper body) or ejected (lower body). The time indicated in each frame is the physical time in the numerical simulation from the instant at which the spheres begin to move.

relative fragment size on the separation process has still not been properly elucidated. It is one of the intents of this paper to address this deficiency.

The separation model proposed by Passey & Melosh (1980) assumes the two fragments, initially lying next to one another, to separate only in the lateral direction. While appropriate for equally sized fragments, this assumption can no longer be considered valid for unequally sized bodies: even if the drag coefficients are identical, the axial accelerations will differ since the aerodynamic force scales with the square of the body radius whereas the mass scales with the radius cubed. Thus, the smaller, or secondary, body travels downstream relative to the larger (primary) body, as well as laterally due to the repulsive effect of the highly compressed gas lying in the region between the two. As the secondary body begins to generate its own bow-shock, a configuration can then develop in which this is intersected by the primary bow-shock ahead of the secondary body. In this situation, the secondary lateral force remains repulsive, however, as the flow on the inner side of the body, having been processed by the primary shock before passing through the secondary shock, experiences a lower stagnation pressure loss than the singly shocked flow on the body's outer side. Thus, the surface pressure on the inner side is higher than that on the outer side. Provided the balance of forces remains correct, the secondary body can then follow, or 'surf', the primary bow-shock downstream.

An example of such surfing is shown in figure 2, depicting a numerical simulation of three spheres of relative sizes 1, 1/2 and 1/4 in a uniform Mach 10 flow. The bow-shock from the primary (largest) sphere initially intersects the shock from each of the two secondary spheres ahead of it: the forces on the larger of the secondary bodies cause it to follow the bow-shock downstream over a considerable distance, gaining significant lateral momentum in the process; the smaller secondary sphere, after surfing a short distance, is entrained within the flow region downstream of the primary shock. The lateral velocity of the larger secondary sphere when it exits the shock results in a value for C in (1.1) of 0.35, which compares with a

https://doi.org/10.1017/jfm.2011.57 Published online by Cambridge University Press

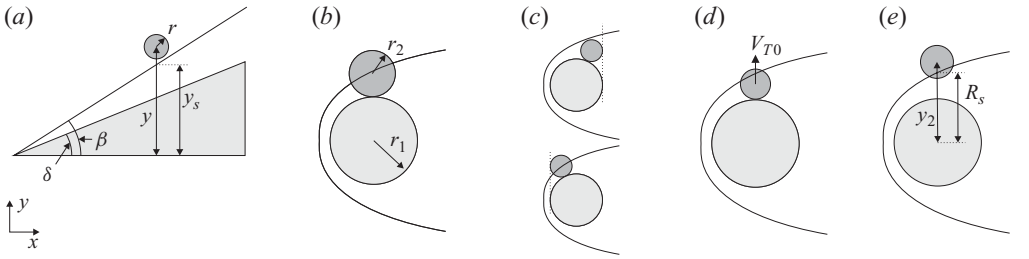


FIGURE 3. Summary of the initial configurations considered in the present work: (*a*) sphere, initially stationary, interacting with wedge-generated oblique shock (relevant to figures 5–11); (*b*) spheres initially stationary and touching, with centres axially aligned (figures 12, 13, 16–18, 23); (*c*) as in (*b*) but with rearmost or frontmost points aligned (figure 19*a*); (*d*) as in (*b*) but with an initial lateral separation velocity (figure 19*b*); (*e*) spheres initially stationary, centres aligned axially but with lateral separation (figures 20–22).

value of 0.04 obtained from a simulation of two equally sized spheres. While these exact values will depend to some extent on the body geometries (note, for example, that Artem'eva & Shuvalov 1996 obtain $C \approx 0.2$ for two symmetrical hemispheres), the physical phenomena that produce the surfing effect are in no way particular to the spherical configuration considered here. Thus, significantly enhanced separation velocities can also be expected for other geometries. It is also clear that the simple r_2/r_1 scaling indicated by (1.1) cannot be considered to hold over a very large range of radius ratios.

This phenomenon may seem superficially similar to the 'surfing' effect referred to earlier, noted by Schultz & Sugita (1994) of small particles within a debris cloud, but the two are fundamentally different. The particle-surfing in the earlier work consists of movement within the shock layer, and always leads to collimation of the particles within the region downstream of the main bow-shock. The present phenomenon results from the special conditions created by the interaction between the primary and secondary bow-shocks, and may lead to the secondary body being either ejected from or entrained within this region.

The simulation shown in figure 2 ran for approximately 62.5 h wall time on a typical PC cluster with 12 quad-core nodes (∼3000 CPU h). Considering the number of parameters that can be varied in this problem, simulations of this size are not a realistic tool for fully exploring the shock-surfing phenomenon. Thus, to aid in the development of an analytical model, in § 3 we first consider a simplified version of the surfing problem, namely a sphere interacting with a planar oblique shock. We verify the proposed analytical model with large-scale, high-resolution computations, the methodology of which is described in § 2. The model is then generalised in § 4 to interactions between two spheres and, after validation of the results with a number of further numerical simulations, used to explore the surfing phenomenon and the separation behaviour in this case. In § 5, a discussion of the significance of these results for the problem of meteoroid fragmentation appears. For the reader's convenience, a schematic summary of the configurations considered in this work is presented in figure 3; for each configuration, the relevant figure numbers are indicated in the caption.

We restrict our attention throughout to spherical geometries in order to avoid the additional complication of induced rotations. The use of such blunt geometries also ensures that viscous contributions to the forces are small; furthermore, the pressure

https://doi.org/10.1017/jfm.2011.57 Published online by Cambridge University Press

on rearward-facing surfaces (relative to the flow direction) on such bodies is negligible in comparison to that on frontward-facing surfaces. This latter point means that, in inviscid simulations, any influence on the separation point on the rear of a body due to the lack of viscous stresses at the wall or through numerical dissipation will have a negligible effect on the integrated forces (although we also note that a significant fraction of the vorticity present in physical hypersonic blunt-body flows is inviscid in nature, being generated by entropy gradients within the curved bow-shock, see Hayes & Probstein 1966). For example, the sphere data collected by Hoerner (1965) show that above a Mach number of approximately 8, the drag force is entirely dominated by the pressure on the front face. The present inviscid treatment is thus justified. The gas is treated as perfect throughout: while real-gas effects, including dissociation, vibrational excitation, radiation and ionisation, are important at the flow conditions relevant to meteoroid entry, the influence of these on the pressure, and thus the forces, is generally limited (see, for example, Vincenti & Kruger 1965 regarding dissociational effects and Artemieva & Shuvalov 2001 regarding radiative and ablative effects).

2. Computational modelling

In this work, we are concerned with supersonic flows undergoing full dynamic interaction with rigid solid bodies. Reliable fluid–structure interaction (FSI) simulations in this regime require the coupling of a shock-capturing fluid dynamics solver for the Euler equations with a rigid-body solver that considers the Newtonian laws of motion. The construction of numerical methods for shock-driven FSI problems is, in itself, still an area of active research, and the number of available software codes is accordingly small. The discretisations for both the fluid flow and the rigid-body dynamics have to be explicit to give time-accurate results, limiting the possible time step size through a Courant–Friedrichs–Lewy (CFL) stability condition. On the other hand, changes in the fluid domain due to the solid body motion need to be accounted for at every time step. Since several thousand explicit FSI time steps will typically have to be computed in a given simulation, a fast mesh or geometry adjustment is vital.

Our approach to this problem is to employ an embedded boundary method in the fluid solver, in which moving solid structures slide through a Cartesian fluid mesh (see figure 4). The structure is represented implicitly with a scalar function that stores in each fluid grid cell the distance to the nearest point on the solid surface. As is characteristic of this approach (called 'level set', cf. Fedkiw *et al.* 1999), the Cartesian finite-volume stencil is itself not modified, which results in a slight diffusion of the boundary location. We alleviate such errors by dynamic adaptive mesh refinement (AMR) of the Cartesian mesh in the vicinity of the embedded boundary. The AMR algorithm and the embedded boundary method are implemented in the AMROC (adaptive mesh refinement in object-oriented C++) code. AMROC is our original development and the software has been used extensively for fully coupled shock- and detonation-driven FSI problems, as described in depth by Deiterding *et al.* (2005), in recent years. Further verification and validation results, which demonstrate the ability of the software to deal with arbitrary structural evolutions while maintaining computational performance and parallel efficiency, are given by Cirak, Deiterding & Mauch (2007) and Deiterding, Cirak & Mauch (2009); validation results for gaseous flows may be found in Deiterding (2005*b*, 2009).

https://doi.org/10.1017/jfm.2011.57 Published online by Cambridge University Press

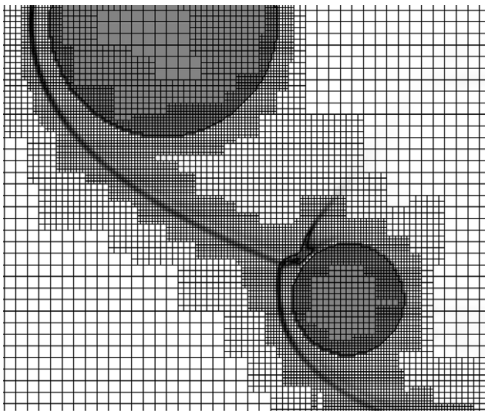


FIGURE 4. Enlarged visualisation of the finite-volume cells in the domain mid-plane for one time step of the computation shown in figure 2. Two additional levels of isotropic refinement, each of factor 2, are employed; the utilisation of refinement patches instead of the refining of individual cells can be clearly inferred. Cells with midpoints within the spherical structures are specially handled, cf. § 2.1.

2.1. *Finite-volume method with embedded boundary treatment*

The governing equations employed to model the inviscid fluid flow are the three-dimensional Euler equations in Cartesian coordinates, written in conservation law form as

$$\frac{\partial}{\partial t}\boldsymbol{q}(\boldsymbol{x},t)+\sum_{n=1}^{3}\frac{\partial}{\partial x_n}\boldsymbol{f}_n(\boldsymbol{q}(\boldsymbol{x},t))=0,\quad \boldsymbol{x}=(x_1,x_2,x_3)^{\mathrm{T}}\in\mathbb{R}^3,\quad t\in\mathbb{R}_0^+, \tag{2.1}$$

with vector of state $\boldsymbol{q}(\boldsymbol{x},t))=(\rho,\rho u_1,\rho u_2,\rho u_3,\rho E)^{\mathrm{T}}$ and flux functions

$$\boldsymbol{f}_n(\boldsymbol{q})=(\rho u_n,\rho u_1u_n+\delta_{1n}p,\rho u_2u_n+\delta_{2n}p,\rho u_3u_n+\delta_{3n}p,u_n(\rho E+p))^{\mathrm{T}}, \tag{2.2}$$

for $n=1,\ldots,3$. Here, ρ is the density, u_n is the nth component of the velocity vector $\boldsymbol{u}$ and E is the specific total energy; δ_{jn} denotes the Kronecker delta and the hydrostatic pressure p is given by the polytropic gas equation of state, $p=(\gamma-1)(\rho E-\rho 1/2\boldsymbol{u}^2)$. We approximate (2.1) with an explicit finite-volume scheme of the form

$$\begin{aligned}\boldsymbol{Q}_{ijk}^{\kappa+1}=\boldsymbol{Q}_{ijk}^{\kappa}&-\frac{\Delta t}{\Delta x_1}\left[\boldsymbol{F}^1_{i+(1/2),jk}-\boldsymbol{F}^1_{i-(1/2),jk}\right]\\&-\frac{\Delta t}{\Delta x_2}\left[\boldsymbol{F}^2_{i,j+(1/2),k}-\boldsymbol{F}^2_{i,j-(1/2),k}\right]-\frac{\Delta t}{\Delta x_3}\left[\boldsymbol{F}^3_{ij,k+(1/2)}-\boldsymbol{F}^3_{ij,k-(1/2)}\right].\end{aligned} \tag{2.3}$$

The numerical flux functions $\boldsymbol{F}^n$ in (2.3) are evaluated with the Van Leer flux vector-splitting method, extended to second-order accuracy with the MUSCL-Hancock method using a minmod-limiter in the primitive variables (see Deiterding 2003 for details). A dimensional splitting approach is used in which three quasi-one-dimensional discrete operators are applied successively, with the data from the preceding sub-step as initial conditions (Toro 1999). In order to incorporate geometrically complex moving boundaries within the Cartesian upwind scheme, we use the nearest layer of finite-volume cells within the structure as ghost cells to enforce immersed boundary conditions (Fedkiw *et al.* 1999). Their values are set immediately before evaluating (2.3) to model moving embedded walls. For the inviscid Euler

https://doi.org/10.1017/jfm.2011.57 Published online by Cambridge University Press

equations, the boundary condition at a rigid wall moving with velocity $\boldsymbol{w}$ is $\boldsymbol{u}\cdot\boldsymbol{n}=\boldsymbol{w}\cdot\boldsymbol{n}$. Enforcing the latter with ghost cells, in which the discrete values are located in the cell centres, requires the mirroring of the primitive values ρ, $\boldsymbol{u}$ and p across the embedded boundary. The normal velocity in the ghost cells is set to $(2\boldsymbol{w}\cdot\boldsymbol{n}-\boldsymbol{u}\cdot\boldsymbol{n})\boldsymbol{n}$, while the mirrored tangential velocity remains unmodified. For details on the construction of the values in embedded ghost cells, including a short discussion of the interpolation operations involved, see Deiterding (2009).

2.2. *Parallel adaptive mesh refinement with fluid–structure coupling*

The dynamic mesh adaptation approach used is the spatial and temporal multi-level AMR algorithm after Berger & Colella (1988), designed specifically for the solution of hyperbolic fluid flow problems. Instead of replacing single cells by finer ones, as is done in cell-oriented refinement techniques, this AMR method follows a patch-oriented approach. Cells flagged by various error indicators are clustered with a special algorithm into non-overlapping rectangular sub-grids, $G_{l,m}$, that define the domain of an entire level $l=0,\ldots,l_{max}$ by $G_l := \cup_{m=1}^{M_l} G_{l,m}$. Refinement is derived recursively from the next coarser level and a hierarchy of successively embedded levels is thereby constructed. All mesh widths on level l are r_l-times finer than on level $l-1$, i.e. $\Delta t_l := \Delta t_{l-1}/r_l$ and $\Delta x_{n,l} := \Delta x_{n,l-1}/r_l$, with $r_l \in \mathbb{N}$, $r_l \geqslant 2$ for $l>0$ and $r_0=1$; thus, a time-explicit scheme remains (in principle) stable under the same stability condition on all levels of the hierarchy. The numerical scheme is applied on level l by calling a single-grid routine implementing (2.3) in a loop over all $G_{l,m}$, which requires the prior setting of a layer of ghost cells around each patch (Deiterding 2003). Specific to the AMROC software is the parallelisation of the AMR algorithm following a rigorous domain decomposition approach, targeting in particular the current generation of distributed memory machines (Deiterding 2005*a*). Load-balanced distributions are re-computed on-the-fly using a hierarchical partitioning algorithm based on a generalised space-filling curve. All computations herein use one to three additional levels of mesh adaptation with refinement factors of either 2 or 3, both in space and in time. Local dynamic refinement is applied up to the highest level available along embedded boundaries and shock waves. Load-balancing and parallel data redistribution are typically carried out every second time step on level zero.

As in our previous work (Laurence *et al.* 2007), we consider only spherical rigid bodies that can be easily embedded into an inviscid fluid flow. It is assumed that even under dynamic motion, these bodies do not come into contact with one another or with an embedded static domain boundary and they are always refined up to the highest level of Cartesian mesh adaptation available. We then update the force $\boldsymbol{f}_\iota(t)$ due to the flow on each of the spheres, indexed ι, after every time step on the highest refinement level. For this purpose, an auxiliary high-resolution longitude–latitude mesh is constructed on each sphere to evaluate the integral fluid pressure. Since the fluid is assumed to be inviscid and the bodies are ideally spherical, rotations can be neglected and only the initial-value problem for the centre of mass, $\ddot{\boldsymbol{x}}_\iota(t)=\boldsymbol{f}_\iota(t)/m_{0,\iota}$, $\boldsymbol{x}_\iota(0)=\boldsymbol{x}_{0,\iota}$, $\dot{\boldsymbol{x}}_\iota(0)=\boldsymbol{v}_{0,\iota}$, using the integral mass $m_{0,\iota}$, the initial sphere position $\boldsymbol{x}_{0,\iota}$, and the initial sphere velocity $\boldsymbol{v}_{0,\iota}$, needs to be solved. We accomplish the latter by applying the forward Euler method twice to each equation of motion. Following a computational splitting approach, the level set function is recomputed after every sphere position update. Since we are considering only non-overlapping bodies of simple geometric shapes, this operation reduces to a straightforward comparison determining the distance to the nearest embedded boundary for each cell midpoint in the Cartesian fluid mesh.

https://doi.org/10.1017/jfm.2011.57 Published online by Cambridge University Press

An exemplary enlarged snapshot of a two-dimensional cut through a three-dimensional AMR computation with embedded spheres is shown in figure 4. The patch-based mesh refinement following the bow-shocks and the embedded boundaries can be clearly inferred.

3. Surfing a planar oblique shock

By replacing the curved primary bow-shock with a planar oblique shock, the complexity of the surfing problem is significantly reduced. The conditions behind the shock are now uniform, so, provided the sphere is sufficiently far from the shock-generating body that reflected shocks have no influence, the only relevant length scale is the sphere radius. Assuming the sphere velocity to be negligible in comparison to that of the free stream, the force coefficients will then depend only on the free-stream Mach number, the shock angle and the position of the sphere relative to the oblique shock. At the Mach numbers of interest here, we may also appeal to the Mach-number independence principle (Hayes & Probstein 1966). Thus, for a given shock angle, the problem can be completely characterised by determining the force coefficients over a range of sphere positions from entirely within to entirely outside the flow region downstream of the oblique shock. Sphere trajectories can then be predicted for arbitrary initial conditions.

The definitive work on the interactions between a blunt body and an oblique planar shock was performed by Edney (1968). Depending on the location of the interaction point, a variety of complex flow configurations can be produced. The most important of these is known as the Edney type IV interaction, in which an impinging supersonic jet produces highly elevated local heating and pressure levels. Edney calculated the individual flow-fields for several configurations, but the complex and varying nature of the shock and shear layer interactions does not lend itself readily to an analysis of the pressure distribution on the body, which is necessary to obtain the desired force coefficients. However, figure 8 of Edney shows that the effect of the impinging structures on the surface pressure distribution is quite localised: away from the impingement point, the pressure soon roughly reverts to the undisturbed profile. Therefore, despite the locally elevated pressure levels, the overall contribution to the integrated forces will be limited (this statement is approximately quantified in § 3.2). This observation is crucial, as it will allow the development of a simple analytical model for the forces acting on the sphere, which can then be generalised to the more complex sphere–sphere case. The smaller parameter space in the present case, however, makes numerical simulation a feasible tool for characterising this problem, and this is the first focus of this section.

3.1. *Computational evaluation of force coefficients*

In this subsection, we employ numerical simulations to calculate the drag and lift coefficients of the spherical body interacting with a planar oblique shock in a fully three-dimensional flow field. In each simulation, the sphere is initially positioned completely inside the flow region downstream of the oblique shock; once the flow is fully established, it is impulsively started with a lateral velocity of 1 % of the free-stream velocity. The aerodynamic forces are calculated by integrating the pressure on the sphere surface at each point along its trajectory. Although the sphere is, in principle, free to respond to the applied forces, since a purely lateral trajectory is desired, the density ratio is set to an artificially high value to ensure that the forces

https://doi.org/10.1017/jfm.2011.57 Published online by Cambridge University Press

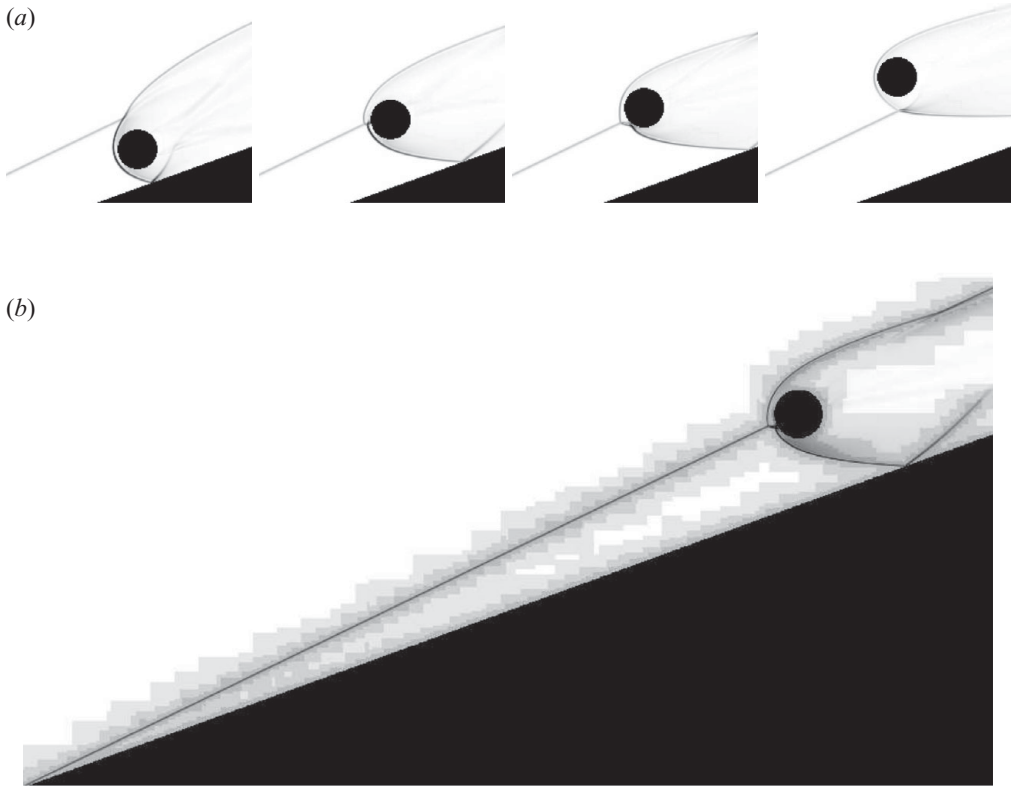


FIGURE 5. (*a*) A sequence of pseudo-Schlieren images, showing the magnitude of the density gradient, of a laterally moving sphere interacting with the oblique shock produced by a 20° wedge at Mach 10; (*b*) a pseudo-Schlieren visualisation of the complete computational domain of the most refined numerical simulation in the refinement study, with the successively embedded domains of additional refinement indicated by grey levels.

do not affect the sphere motion. The computation is concluded once the sphere has completely exited the influence of the oblique shock.

All computations of the sphere/oblique-shock configuration employ a free-stream Mach number of 10. The oblique shock is generated by a wedge forming the lower boundary of the computational domain. The extent of the domain depends on the wedge angle, δ: for $\delta = 20°$, for example, the base grid is $200 \times 140 \times 20$ cells, corresponding to a physical domain of $20 \times 14 \times 2$ sphere diameters. Two levels of additional refinement are applied, each of factor 2; thus, at the highest level the sphere diameter comprises 40 cells. A rather conservative CFL number of either 0.7 or 0.8 is used to avoid excessive re-evaluation of otherwise unstable steps when using dynamic time-step adjustment. All computations were run on 32 quad-core nodes of an IBM BG/P machine: the $\delta = 20°$ simulation, for instance, required $\sim$61.7 h wall time ($\sim$7900 CPU h) and 18 112 time-step updates computed on the finest level. In figure 5 is presented a sequence of computational pseudo-Schlieren images from this simulation.

In order to quantify the accuracy of the determined force coefficients at the level of the resolution employed, a refinement study was carried out for a wedge angle of 20°. Up to three additional levels of refinement were applied over the base grid, with all

https://doi.org/10.1017/jfm.2011.57 Published online by Cambridge University Press

Additional levels	r.m.s. change (%) C_D	C_L
0–1	2.6	7.4
1–2	1.4	4.3
2–3	0.7	2.8

TABLE 1. Results of the refinement study, tabulated as the normalised r.m.s. difference between the force coefficients at consecutive levels of refinement.

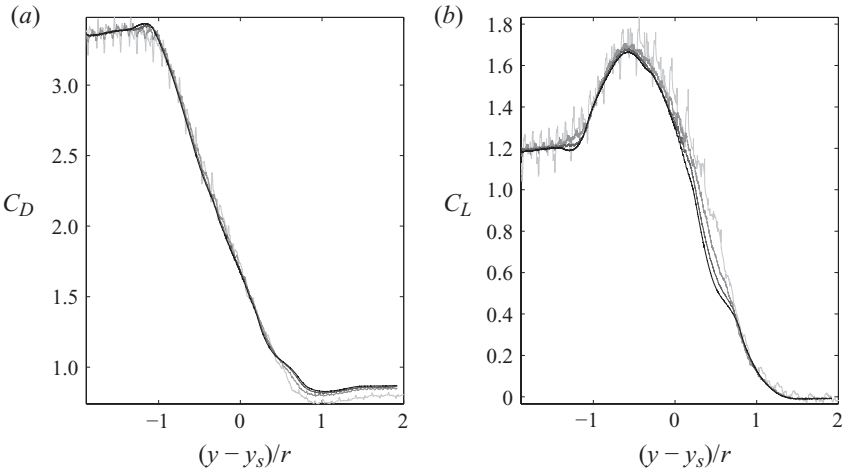


FIGURE 6. Results of the refinement study, showing the drag (*a*) and lift (*b*) coefficients for 0–3 (lightest to darkest) levels of additional refinement over the base grid.

other computational parameters remaining identical. The most refined computation required approximately 16.4 days wall time to finish on 32 quad-core nodes of the IBM BG/P (∼50 250 CPU h), taking 36 344 time-step updates on the finest level. Note that on a uniform grid, the computational expense would increase by $2^4 \equiv 16$ whenever the resolution were doubled. A visualisation of the entire computational domain from this computation, showing both the magnitude of the density gradient and the refinement strategy, is presented in figure 5. Even at this refinement level, the impinging shock structures are not fully resolved; however, increasing the refinement further would be prohibitive in terms of computational cost, and perhaps fruitless insofar as the influence of numerical viscosity would become important at the smallest scales.

Results of the refinement study are shown in figure 6: the drag and lift coefficients for each level of refinement are plotted against the normalised lateral displacement of the sphere centre from the shock position (the nature of these coefficient profiles is discussed more fully in the following paragraph). The drag profiles are essentially converged at the highest two levels; there remain small differences in the corresponding lift profiles, but overall convergence may be considered adequate. These results are further summarised in table 1, in which the root-mean-square (r.m.s.) percentage differences between consecutive levels are tabulated. These differences are seen to progressively decrease in magnitude as the refinement level is increased, though the

https://doi.org/10.1017/jfm.2011.57 Published online by Cambridge University Press

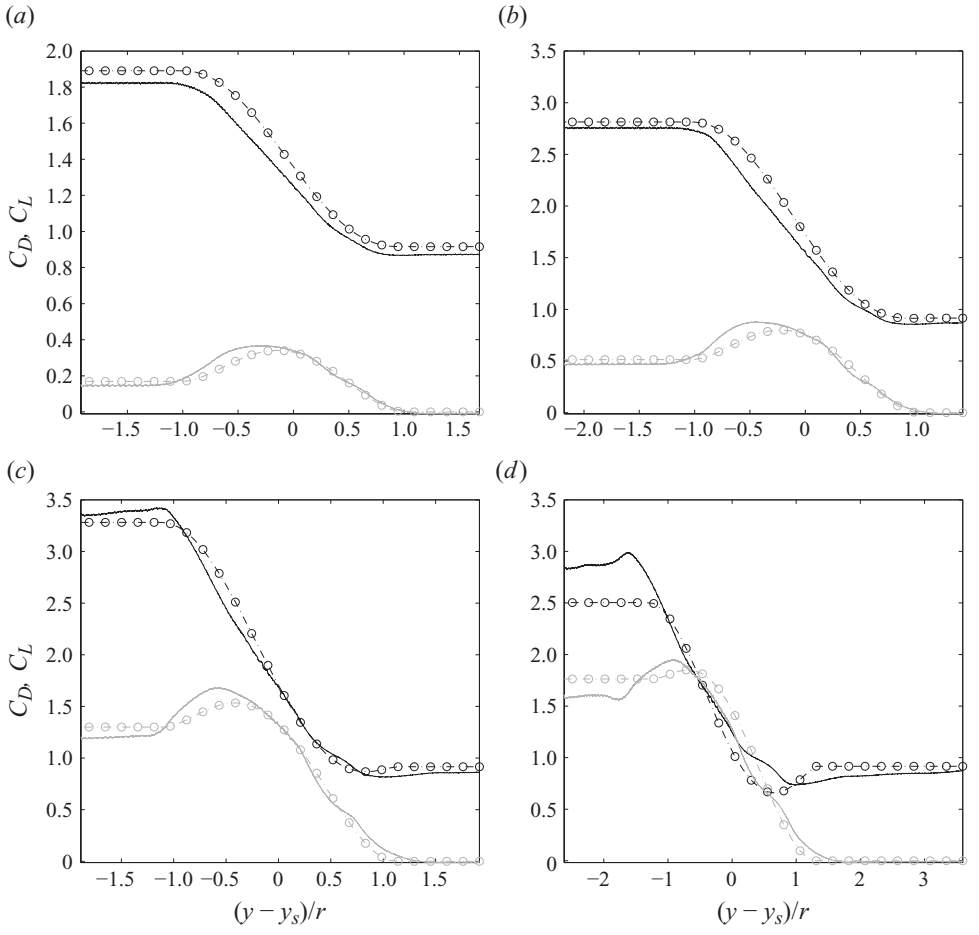


FIGURE 7. Computational (—) and analytical (– · –○– · –) force coefficients – (dark) drag, (light) lift – for a sphere interacting with a planar oblique shock. The wedge angles are 5°, 10°, 20° and 30° (*a–d*, respectively). The abscissa in each case is the normalised lateral displacement from the shock.

lift is again slightly more sensitive to changes in refinement at the highest levels (this is partly due to the lower mean value of the lift coefficient). It may be concluded from these results that even though the computations are unable to fully resolve the impinging shock structures, the effect on the calculated force coefficients is unlikely to be problematic. Furthermore, the use of two additional refinement levels (as in all other computations described in this section) gives satisfactory accuracy in the calculated force coefficients.

The computed drag and lift coefficients for wedge angles of 5°, 10°, 20°, and 38.5°, respectively, are plotted in figure 7. Also plotted are analytical profiles, discussed in the following subsection. The abscissa in each case is the lateral displacement (normal to the free-stream flow direction) normalised by the sphere radius, r, with the origin being the point at which the plane of the shock passes through the sphere centre. Reading from right to left, corresponding to movement from outside to inside the region downstream of the shock, the drag shows a small dip as the sphere begins to intersect with the shock, then rises monotonically, with a small overshoot for larger

https://doi.org/10.1017/jfm.2011.57 Published online by Cambridge University Press

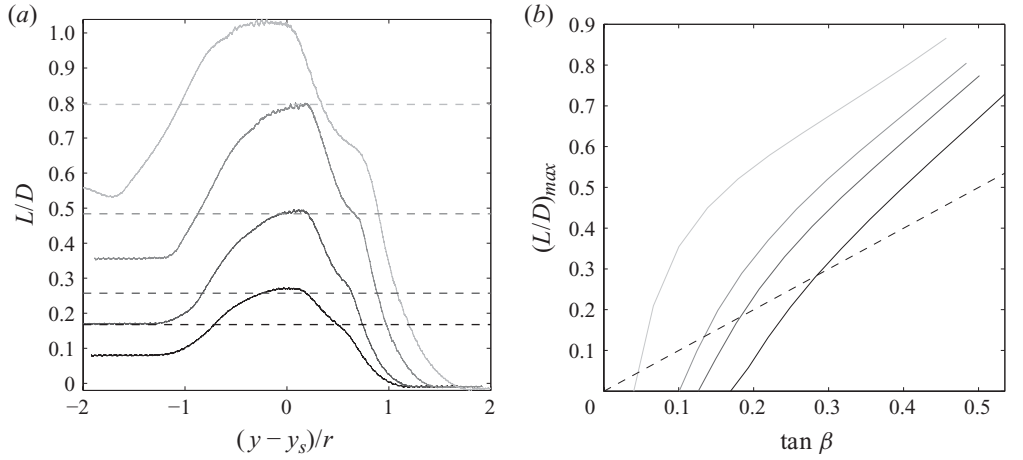


FIGURE 8. (*a*) Ratio of lift to drag for sphere/oblique-shock interactions, with wedge angles of 5°, 10°, 20° and 30° (dark to light). The horizontal dashed line for each shade indicates the tangent of the corresponding shock angle. (*b*) The maximum L/D value versus the tangent of the shock angle for Mach numbers of (dark through light) 6, 8, 10 and 25, as predicted by the analytical model. The dashed line corresponds to $(L/D)_{max} = \tan\beta$.

wedge angles, until the sphere is fully immersed in the region behind the shock. The lift also rises rapidly once the interaction begins, but reaches a well-defined maximum before decreasing to its fully immersed value. Note that, over a broad range of wedge angles ($10° \lesssim \delta \lesssim 30°$), the drag profiles show relatively little variation, with the maximum immersed drag occurring at $\delta \approx 20°$; however, the lift profiles vary strongly, with larger wedge angles producing significantly higher maximum lift values.

The lift/drag ratios from these simulations are plotted against the normalised lateral displacement in figure 8(*a*), together with horizontal lines indicating the tangent of the shock angle in each case. For each wedge angle, this line is seen to intersect the L/D curve in two places. Thus, if the sphere is placed with zero initial velocity at a lateral displacement corresponding to either of these two points, it will remain in the same position relative to the shock as it accelerates, surfing the shock downstream over the length of the wedge (assuming that the sphere velocity remains negligible compared with the flow velocity). However, only one of these stationary points (that corresponding to a positive $(y - y_s)/r$) is stable. For the other, a small decrease in y will lead to a decreased L/D, and the sphere will move further in this direction; on the other hand, a small increase in y will lead to an L/D greater than $\tan\beta$, and the sphere will be further repulsed. In general, provided the maximum L/D value, $(L/D)_{max}$, is greater than $\tan\beta$ (this condition is discussed shortly), there will always be two such stationary points. This follows from the fact that, in the free stream, $L/D = 0$, whereas inside the region downstream of the shock, $L/D = \tan\delta$. As $\tan\delta < \tan\beta$, provided $(L/D)_{max} > \tan\beta$, the L/D profile must intersect the $\tan\beta$ line (at least) twice.

3.2. *Theoretical modelling of force coefficients*

Given the limited parameter space in sphere-wedge configurations, numerical simulations are a suitable tool for exploring this problem. However, it is of interest to see whether a simple analytical model can yield reasonable results as the development of such a model will be necessary to fully explore the more complex sphere–sphere

https://doi.org/10.1017/jfm.2011.57 Published online by Cambridge University Press

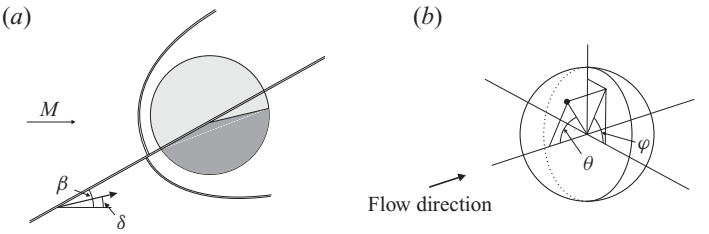


FIGURE 9. (*a*) Approximation to the flow over the sphere used for the analytical model: the planar shock is assumed to divide the flow over the sphere into two distinct regions, but producing no interaction with the sphere bow-shock. The flow angle rather than the shock angle is used as the dividing plane on the rear half of the sphere. (*b*) Definition of angles for calculation of the pressure distribution on the sphere.

problem. We begin then, as shown in figure 9(*a*), by ignoring the complicated shock and shear-layer interactions near the shock intersection point, and assume that the oblique shock acts only to divide the flow over the sphere into two separate regions. A rough justification for doing this, appealing to the localised effects of impinging flow structures shown in figure 8 of Edney (1968), was given earlier. In each of these regions, we model the surface pressure using the modified Newtonian distribution (Lees 1955):

$$p = \begin{cases} (p_{02} - p_1)\cos^2\psi + p_1, & \text{for } \psi \in [0, \pi/2), \\ p_1, & \text{for } \psi \in [\pi/2, \pi), \end{cases} \tag{3.1}$$

where, in the flow region upstream of the oblique shock, $\psi = \theta$ (the zenith angle of the sphere), and downstream, $\cos\psi = \cos\theta\cos\delta - \sin\theta\sin\varphi\sin\delta$, where φ and δ are the azimuthal and flow deflection angles, respectively. The convention used here is shown in figure 9(*b*). The static pressure, p_1, is either the free-stream static pressure, p_a, or calculated from p_a using the oblique shock relations; the Pitot pressure, p_{02}, is obtained in ratio to p_1 using the Rayleigh–Pitot formula. The drag and lift coefficients can be written as

$$C_D = \frac{2}{\gamma\pi r^2 M^2}\int_S \frac{p}{p_a}\cos\theta\,\mathrm{d}S, \tag{3.2}$$

$$C_L = -\frac{2}{\gamma\pi r^2 M^2}\int_S \frac{p}{p_a}\sin\theta\sin\varphi\,\mathrm{d}S, \tag{3.3}$$

where S denotes the sphere surface; we have used the relation $\rho_a V^2 = \gamma p_a M^2$, M being the Mach number and γ the ratio of specific heats. The force coefficients are then easily calculated by numerical integration, with p/p_a determined by (3.1). Note that, as shown in figure 9, on the rear half of the sphere the flow angle rather than the shock angle is used as the dividing plane between the two flow regions. While this makes little difference for smaller wedge angles ($\delta \leqslant 20^\circ$), the use of the shock angle for larger δ was found to lead to an unrealistically low drag coefficient when the shock intersection point lay towards the inner side of the sphere.

In figure 7, the force coefficients obtained using this approximate model are compared with the computational profiles described earlier. At the largest wedge angle, $\delta = 30^\circ$, the main features of the profiles are similar, but quantitative agreement is lacking. This is because the modified Newtonian result, while giving a good prediction for the pressure distribution at large Mach numbers, becomes increasingly approximate as the Mach number is decreased. The post-shock Mach number for the

https://doi.org/10.1017/jfm.2011.57 Published online by Cambridge University Press

	C_D		C_L	
Wedge angle	r.m.s.	Maximum	r.m.s.	Maximum
5°	0.06	0.15	0.16	0.07
10°	0.07	0.28	0.13	0.16
20°	0.05	0.18	0.10	0.25
30°	0.14	0.48	0.13	0.16

TABLE 2. Quantification of the discrepancies between the computationally obtained and analytically derived force coefficient profiles shown in figure 7. The r.m.s. difference is normalised by the mean of the computational profile in each case; the maximum difference is the absolute un-normalised maximum value.

30° wedge is 2.7, low enough that errors in the Newtonian result become significant. However, for wedge angles of 20° (for which the post-shock Mach number is 4.2) or less, agreement is satisfactory. The most notable discrepancy at these smaller wedge angles is an underprediction of the lift coefficient between $(y - y_s)/r = -0.25$ and -1, i.e. when the shock intersection point lies ahead of the outer side of the sphere. The differences between the computational and analytical results are quantified in table 2. For each wedge angle, both normalised r.m.s. and un-normalised absolute maximum differences are given. The discrepancy in the drag is seen to lie in the range 5 %–7 %, except for the largest wedge angle where it rises to 14 %. The lift discrepancy is somewhat higher, at around 13 %, in part due to the lower mean value of the lift coefficient. Although these differences cannot be entirely attributed to the neglecting of the shock interactions in the analytical model (note, for example, that there is a drag offset even in the free stream), we may reasonably conclude that these interactions have only a limited influence on the drag and lift coefficients.

In the previous subsection, we noted that the sphere can follow the oblique shock downstream provided $(L/D)_{max} \geqslant \tan\beta$. While we might predict from first principles that the minimum β for this condition to hold will increase with decreasing Mach number, the analytical model provides a convenient method for obtaining an approximate quantitative prediction. In figure 8(*b*) is plotted $(L/D)_{max}$ against $\tan\beta$ for four Mach numbers between Mach 6 and 25. The point at which each curve crosses the $(L/D)_{max} = \tan\beta$ line indicates the minimum β for which stable shock-following, i.e. surfing, is possible at that Mach number. For $M = 25$, surfing is possible over almost the entire range of β down to the Mach angle (at which $(L/D)_{max} = 0$). As the Mach number is decreased, however, the range of such β becomes more limited: at $M = 6$, a minimum β for stable surfing of 16° is predicted. The analytical model cannot be expected to give accurate results below this Mach number, but we can safely predict that this minimum β will continue to increase for lower M.

3.3. *Utilisation of force coefficients to predict sphere dynamics*

From the computational drag and lift profiles shown in figure 7, sphere trajectories for various initial positions can be calculated by integrating the set of differential equations:

$$\frac{\mathrm{d}\hat{x}}{\mathrm{d}\hat{t}} = \hat{v}_x, \quad \frac{\mathrm{d}\hat{y}}{\mathrm{d}\hat{t}} = \hat{v}_y, \quad \frac{\mathrm{d}\hat{v}_x}{\mathrm{d}\hat{t}} = \frac{3}{8}C_D(\hat{x}, \hat{y}), \quad \frac{\mathrm{d}\hat{v}_y}{\mathrm{d}\hat{t}} = \frac{3}{8}C_L(\hat{x}, \hat{y}), \tag{3.4}$$

where $\hat{x} = x/r$ and $\hat{y} = y/r$ are the non-dimensional axial and lateral coordinates. Also, $\hat{t} = \sqrt{\rho_a/\rho_m}tV/r$ is the non-dimensional time, and $\hat{v}_x = \sqrt{\rho_m/\rho_a}v_x/V$ and

https://doi.org/10.1017/jfm.2011.57 Published online by Cambridge University Press

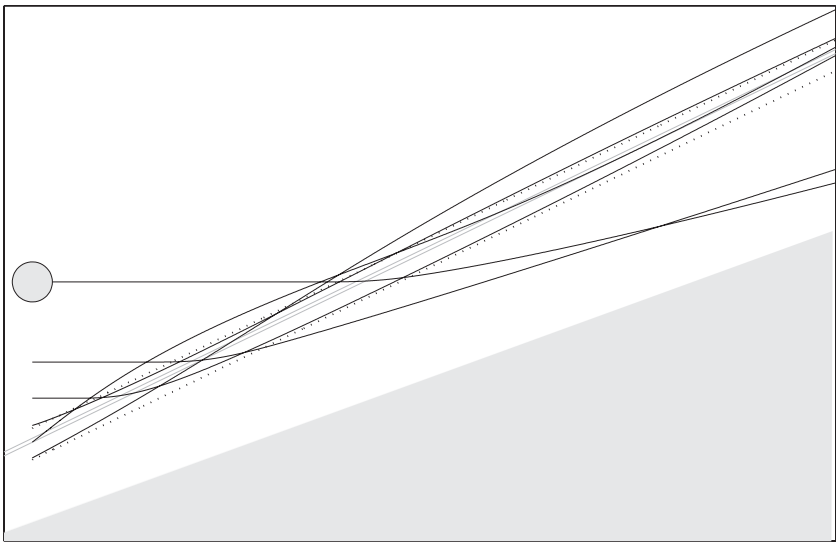


FIGURE 10. Sphere trajectories for various initial positions and zero initial velocity with $\delta = 20°$. The shock is indicated by the double grey line, and the stationary points (relative to the shock) by dotted lines.

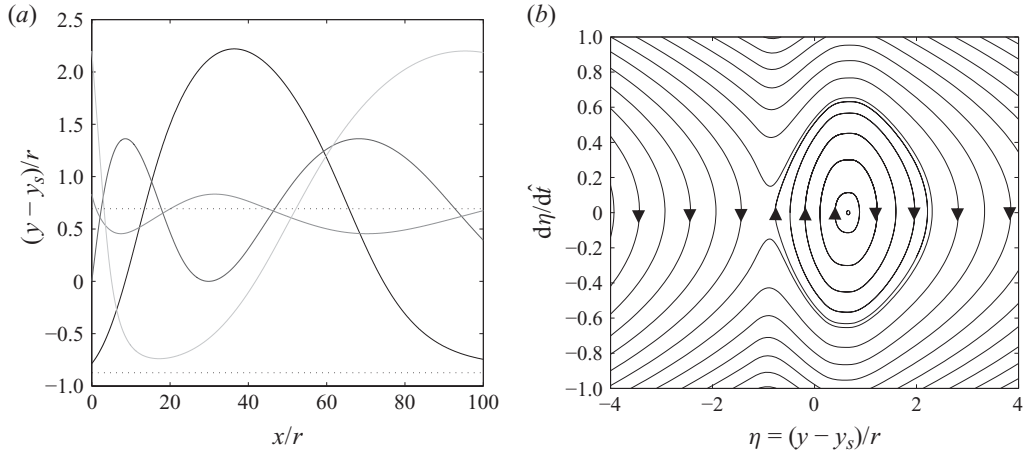


FIGURE 11. Sphere trajectories for $\delta = 20°$: (*a*) in normalised coordinates and (*b*) in the phase plane. The dotted lines in (*a*) indicate the stationary points in the phase diagram.

$\hat{v}_y = \sqrt{\rho_m/\rho_a}\, v_y/V$ are the non-dimensional axial and lateral sphere velocities, respectively. These trajectories may be considered valid as long as the sphere speed remains negligible compared with the flow speed ahead of the sphere (a criterion that will depend on the density ratio, ρ_m/ρ_a). Several trajectories in physical space for a wedge angle of 20° are plotted in figure 10; these are reproduced with the lateral coordinate calculated relative to the shock position, y_s, in figure 11(*a*) (the trajectories that penetrate completely into the region downstream of the oblique shock are omitted here). For clarity, we have limited ourselves here to $\hat{v}_x(0) = \hat{v}_y(0) = 0$. The stationary points (at which $L/D = \tan\beta$) are indicated by dotted lines in both plots. The contrasting stability of the two stationary points is immediately apparent: a trajectory starting close to the inner point is quickly expelled into the

https://doi.org/10.1017/jfm.2011.57 Published online by Cambridge University Press

free stream, whereas another starting close to the outer point oscillates around the shock.

The existence of such stationary points and the oscillatory nature of the sphere trajectories suggest that the sphere dynamics could be further elucidated by a phase-plane analysis. Noting then that $C_D(\hat{x}, \hat{y}) = C_D(\hat{y} - \hat{y}_s) = C_D(\hat{y} - \tan\beta\,\hat{x})$, and similarly for C_L, defining $\eta = \hat{y} - \tan\beta\,\hat{x}$, the system of (3.4) can be reduced to

$$\frac{\mathrm{d}\eta}{\mathrm{d}\hat{t}} = v_\eta, \qquad \frac{\mathrm{d}v_\eta}{\mathrm{d}\hat{t}} = \frac{3}{8}\left[C_L(\eta) - \tan\beta\, C_D(\eta)\right], \tag{3.5}$$

where $v_\eta = \hat{v}_y - \tan\beta\,\hat{v}_x$. The phase diagram of (3.5) for $\delta = 20^\circ$ is shown in figure 11(*b*). The stationary points, both lying at $v_\eta = 0$, are seen to be a centre and a saddle point, respectively; in fact, this phase diagram is very similar to that of a simple pendulum. The bounding neutrally stable orbit indicates the range of initial conditions for which the sphere follows the shock downstream; the sphere trajectories in this region will oscillate around the stable stationary point with growing wavelengths but no change in amplitude, due to the lack of damping terms in (3.5). For all initial conditions lying outside this orbit, the sphere will penetrate fully into the region downstream of the shock and remain there. The range of η for shock-following is maximum at $v_\eta = 0$, extending from the saddle point at $\eta = -0.88$ to $\eta = 2.2$. The phase portraits for other wedge angles are qualitatively similar to that shown: the positions of the stationary points on the $v_\eta = 0$ axis vary slightly, as may be inferred from figure 8(*a*), but all other features are identical.

The nature of the stationary points may also be deduced by considering the eigenvalues of the Jacobian of (3.5). These are easily shown to be

$$\lambda = \pm\sqrt{\frac{3}{8}\left(\frac{\mathrm{d}C_L}{\mathrm{d}\eta} - \tan\beta\frac{\mathrm{d}C_D}{\mathrm{d}\eta}\right)}. \tag{3.6}$$

Noting from the quotient rule that

$$\frac{\mathrm{d}}{\mathrm{d}\eta}\left(\frac{C_L}{C_D}\right) = \frac{1}{C_D^2}\left(C_D\frac{\mathrm{d}C_L}{\mathrm{d}\eta} - C_L\frac{\mathrm{d}C_D}{\mathrm{d}\eta}\right) = \frac{1}{C_D}\left(\frac{\mathrm{d}C_L}{\mathrm{d}\eta} - \frac{C_L}{C_D}\frac{\mathrm{d}C_D}{\mathrm{d}\eta}\right), \tag{3.7}$$

and that, at the stationary points, $C_L/C_D = \tan\beta$, we have

$$\lambda = \pm\sqrt{\frac{3}{8}C_D\frac{\mathrm{d}}{\mathrm{d}\eta}\left(\frac{C_L}{C_D}\right)}, \tag{3.8}$$

where C_D and the derivative are evaluated at the relevant point. As $C_D > 0$, by equating η with $(y - y_s)/r$ in figure 8 we see that, at the inner (i.e. $\eta < 0$) stationary point, $\mathrm{d}(C_L/C_D)/\mathrm{d}\eta > 0$; hence, λ are real and of opposite sign, indicating this to be a saddle point. At the outer stationary point, $\mathrm{d}(C_L/C_D)/\mathrm{d}\eta < 0$; hence, the eigenvalues are imaginary, indicating that the stationary point in the linearised system is a centre. While it cannot be concluded immediately that the corresponding point in the original system is a centre (as a centre in the linearised system may correspond to a stable or unstable node in the nonlinear system), this may be deduced from the absence of damping terms in (3.5).

4. Surfing with spheres

We now turn to the sphere–sphere problem, more representative of the situation encountered in meteoroid fragmentation. A sense of the important role that the radius

https://doi.org/10.1017/jfm.2011.57 Published online by Cambridge University Press

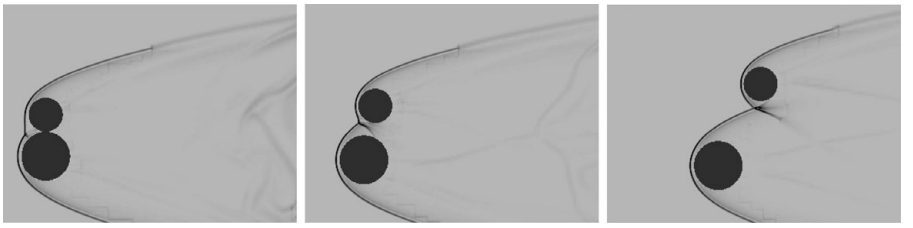


FIGURE 12. Pseudo-Schlieren images (based on the magnitude of the density gradient) showing the computed separation of two initially touching spheres of radius ratio 0.7 at Mach 10.

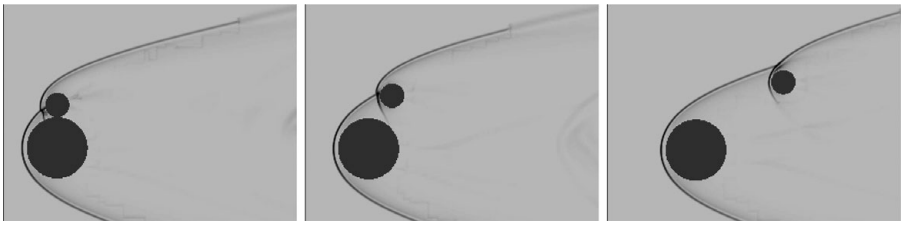


FIGURE 13. Pseudo-Schlieren images showing the computed separation of two spheres of radius ratio 0.4 at Mach 10.

ratio plays in determining the separation process may be gained by comparing the visualisation sequences in figures 12 and 13, showing the simulated separations of initially touching sphere pairs with radius ratios of 0.7 and 0.4, respectively, and that of the $r_2/r_1 = 0.5$ case in figure 2. For $r_2/r_1 = 0.7$, surfing takes place over only a short distance and a separation velocity corresponding to $C = 0.14$ in (1.1) results (compared to $C = 0.35$ and 0.04 for $r_2/r_1 = 0.5$ and 1, respectively). For $r_2/r_1 = 0.4$, the secondary sphere is quickly entrained within the region downstream of the primary shock, with a maximum lateral velocity corresponding to $C = 0.06$. It is apparent that there exists some critical radius ratio in the range $0.4 \leqslant r_2/r_1 \leqslant 0.5$ that delineates entrainment from expulsion for this initially touching configuration. This critical ratio will be the value at which the surfing distance is maximum and the separation velocity close to maximum.

A number of numerical simulations of the two-sphere configuration were carried out and are described in § 4.2. However, if, in addition to the radius ratio, both the initial relative positions and velocities of the bodies are allowed to vary, the parameter space of the problem becomes too large to explore computationally; the smallest value of r_2/r_1 and the extent of the physical domain that can be investigated with numerical simulations are also limited. Thus, the following subsection is concerned with developing an analytical model to determine the interacting force coefficients in the two-sphere surfing problem.

4.1. *Analytical modelling*

We begin as in the sphere-wedge case, now appealing to the results discussed in § 3.2, by ignoring the complex flow structures near the shock interaction point and by assuming that the primary shock acts, as shown in figure 9, simply to divide the flow over the secondary sphere into two regions (note that the shock angle rather than the flow angle is now used on the rear half of the sphere). The outer region, exposed to the free-stream flow, is modelled as before with the modified Newtonian pressure distribution. Owing to the non-uniformity of the flow conditions behind the primary

https://doi.org/10.1017/jfm.2011.57 Published online by Cambridge University Press

bow-shock, however, dealing with the inner region is now more difficult. Assuming the shock angle is known, the flow conditions immediately behind the shock are also known, but approximations must be made further inside the region downstream of the shock.

In Laurence *et al.* (2007), it was shown that the hypersonic blast-wave analogy, when combined with the modified Newtonian theory, gives a good approximation to the forces, and, by extension, the pressure distribution, acting on a spherical secondary body fully inside the flow region bounded by the bow-shock of a primary sphere. Thus, here we use a similar idea for the inner side of the secondary sphere: the pressure at any point on the surface is assumed to follow the modified Newtonian result (3.1) with the Pitot pressure and the flow direction corresponding to the local conditions in the blast-wave solution. The blast-wave results are modified slightly, however, in the form of a scaling that takes into account the conditions known immediately behind the shock (through the oblique shock relations). The static pressure, for example, is given by $p = p_{bw}(x, y)p_{os}(M, \beta)/p_{bw}(x, R_s)$, where p_{bw} and p_{os} are respectively the blast-wave and oblique shock pressures, and $R_s(x)$ is the radial location of the shock, which, along with the shock angle $\beta(x)$, is assumed to be known; x and y are the axial and lateral coordinates, respectively. The use of the oblique shock relations is intended to address the limited range of validity of the blast-wave solution at finite Mach numbers, in particular at distances downstream for which the strong shock assumption, $M \sin\beta \gg 1$, can no longer be considered valid (see, for example, Laurence 2006).

With the pressure distribution thus defined, the drag and lift coefficients can be calculated by integrating it over the surface of the secondary body, as before. To simplify the integration, the following approximation to the blast-wave solution is made. While an analytical solution to this problem is available (Sedov 1959), it is not an explicit relation for the flow variables. In particular, the relation between the non-dimensional lateral flow velocity, $\hat{u} = (\gamma+1)u/(yV/x)$, and the similarity variable, $\eta \propto y/\sqrt{x}$, is

$$\left(\frac{\eta_0}{\eta}\right)^2 = \hat{u}(\gamma + 1 - \gamma\hat{u})\left(\frac{2\gamma\hat{u} - \gamma - 1}{\gamma - 1}\right)^{-(\gamma-1)/\gamma}, \tag{4.1}$$

where $\eta/\eta_0 = y/R_s$. The non-dimensional density and pressure are both functions of $\hat{u}$ and γ alone. However, the product $\hat{u}(\gamma + 1 - \gamma\hat{u})$ in (4.1) is very close to unity; thus, a good approximation to $\hat{u}$ is given by

$$\hat{u} = \frac{1}{2\gamma}[(\gamma - 1)(\eta/\eta_0)^{2\gamma/(\gamma-1)} + \gamma + 1]. \tag{4.2}$$

Plots of the approximate and exact solutions are shown in figure 14; considering the other simplifications made in the analytical model, agreement is certainly close enough to justify the use of this approximation.

4.2. *Numerical simulations*

To gauge the performance of the analytical model, a set of numerical simulations of the two-sphere problem was performed. The simulations are of two types. In the first, the computational methodology is similar to that described in § 3, but with a fixed primary sphere replacing the wedge. The secondary sphere is initially positioned completely inside the region downstream of the primary shock, and, once the flow is established, is impulsively started with a lateral velocity of 1 % of the free-stream velocity. The forces are calculated numerically at each point along the lateral trajectory

https://doi.org/10.1017/jfm.2011.57 Published online by Cambridge University Press

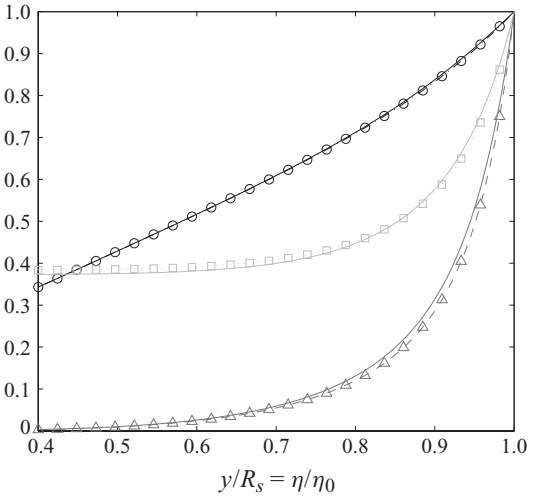


FIGURE 14. Similarity solution to the axisymmetric blast-wave problem: (solid) exact solution; (symbols) approximation using (4.2). The flow variables are: ○, u/u_s; △, ρ/ρ_s; □, p/p_s, where the subscript s refers to conditions immediately behind the shock.

until the sphere is completely free of the influence of the shock. In the second group of simulations, examples of which are shown in figures 12 and 13, the spheres initially touch one another and, once the flow is established, are released at the same instant with zero initial velocities and subsequently allowed to move freely according to the forces experienced. These latter computations are intended to test the ability of the analytical model to simulate the fragment separation problem, whereas the first group was performed to give a more complete picture of the performance of the analytical model in predicting the interacting secondary forces.

Details of the computations are as follows. For the impulsively started simulations, the size of the computational domain depends on the downstream displacement of the secondary sphere. The maximum displacement considered is 4 primary sphere diameters (centre-to-centre), for which the base grid is $130 \times 100 \times 50$, corresponding to a physical domain of $6.5 \times 5.0 \times 2.5$ primary diameters. In the majority of the simulations (for which $r_2/r_1 = 0.5$), two additional levels of refinement of factor 2 are used, resolving the primary diameter to 80 cells at the highest level. For the single $r_2/r_1 = 0.25$ simulation, a refinement factor of 3 at the highest level is employed. For all impulsively started simulations, the Mach number is 25 and the CFL number 0.8. The computational overhead depends on the particular geometry: the simulation with the largest physical domain ran for ∼103.5 h wall time on 256 cores of the IBM BG/P machine (∼26 200 CPU h), performing 34 396 time steps on the finest level.

For the free-flying simulations, a base grid of $130 \times 105 \times 50$, corresponding to a physical domain of $6.5 \times 5.25 \times 2.5$ primary diameters, is employed with a single level of refinement of factor 3. At the refined level, the effective diameter of the primary sphere is 60 cells. The density ratio, ρ_m/ρ_a, is 1000, which is a compromise between computational time and a desire for the maximum sphere velocities to remain sufficiently low that the results can be considered independent of ρ_m/ρ_a. This choice of value means that the maximum velocity of the secondary sphere is typically limited to 10 % of the free-stream velocity during the time period of interest. A CFL number

https://doi.org/10.1017/jfm.2011.57 Published online by Cambridge University Press

of 0.8 is used throughout; each computation ran for ∼50 h wall time on two cores of a quad-core 2.8 GHz Linux workstation. Two Mach numbers of 10 and 25 are considered and, for each, the radius ratio is varied over a range of values between 0.3 and 1. For all free-flying computations, the spheres are initially positioned with their centres at the same axial location and with their lateral edges just touching (figure 3*b*).

4.3. *Comparison of analytical and computational results*

In this subsection, we assess the performance of the analytical model by comparing its predictions with the results of the numerical simulations just described. To provide an appropriate comparison, the primary shock profile in the analytical calculations was specified using a polynomial curve-fit to the computational shock. The surface dividing the flow regions on the secondary body in the analytical model was calculated according to the shock angle at the point of intersection with the sphere; the shock was then assumed to be planar in the axial direction, but shock curvature in the transverse direction was accounted for. In the free-flying simulations, since the analytical model does not provide any means of predicting the motion of the primary body, this was taken in each case from the corresponding computation (except for the $r_2 = r_1$ case, for which symmetry could be used). Less *ad hoc* methods for dealing with the primary shock shape and the primary body motion are discussed later in this article.

In figure 15 are presented computational and analytical results from the impulsively started simulations. The drag and lift coefficients are plotted against the normalised lateral displacement from the shock (with R_s being the effective radial shock location at the axial displacement of the secondary sphere centre). The computational profiles for $y - R_s > 0$ are seen to be similar to the corresponding sphere-wedge curves shown in figure 7. As the secondary body moves further inside the region downstream of the primary shock, however, the sharply decreasing flow density (see figure 14) means that the forces quickly drop away from their peak values, with the drag coefficient now also achieving a well-defined maximum. An extensive analysis of the nature of the forces within this region may be found in Laurence *et al.* (2007). Agreement between analytical and computational results is satisfactory, especially considering the number of simplifying assumptions in the analytical model. The most noticeable discrepancy is the analytical prediction for the magnitude of the forces to drop more rapidly for $y - R_s < 0$. A similar effect was observed in Laurence *et al.* (2007), and was attributed to the strong entropy wake in the blast-wave approximation.

Turning now to the free-flying simulations, analytical and computational trajectories for two cases, $r_2/r_1 = 0.5$ and 0.6, both at $M = 25$, are shown in figure 16, and the x- and y-displacements as functions of time are plotted for the smaller radius ratio in figure 17. From these displacement profiles, it is clear that the analytical model underpredicts both the drag and the lift in the early stages of the motion, when there is only a small separation between the spheres. This was also clear from a comparison of the analytical and numerical forces, and is not surprising: not only is the initial shock angle sufficiently large (∼40°) that the results of the analytical model are questionable even for the simpler sphere-wedge configuration (see figure 7), but, in addition, in the physical flow field there is a region of highly compressed gas between the two bodies that augments both the lift and the drag; this feature is not present in the analytical model. In spite of this initial discrepancy, however, the computational and analytical trajectories lie close to one another, indicating that at least the ratio

https://doi.org/10.1017/jfm.2011.57 Published online by Cambridge University Press

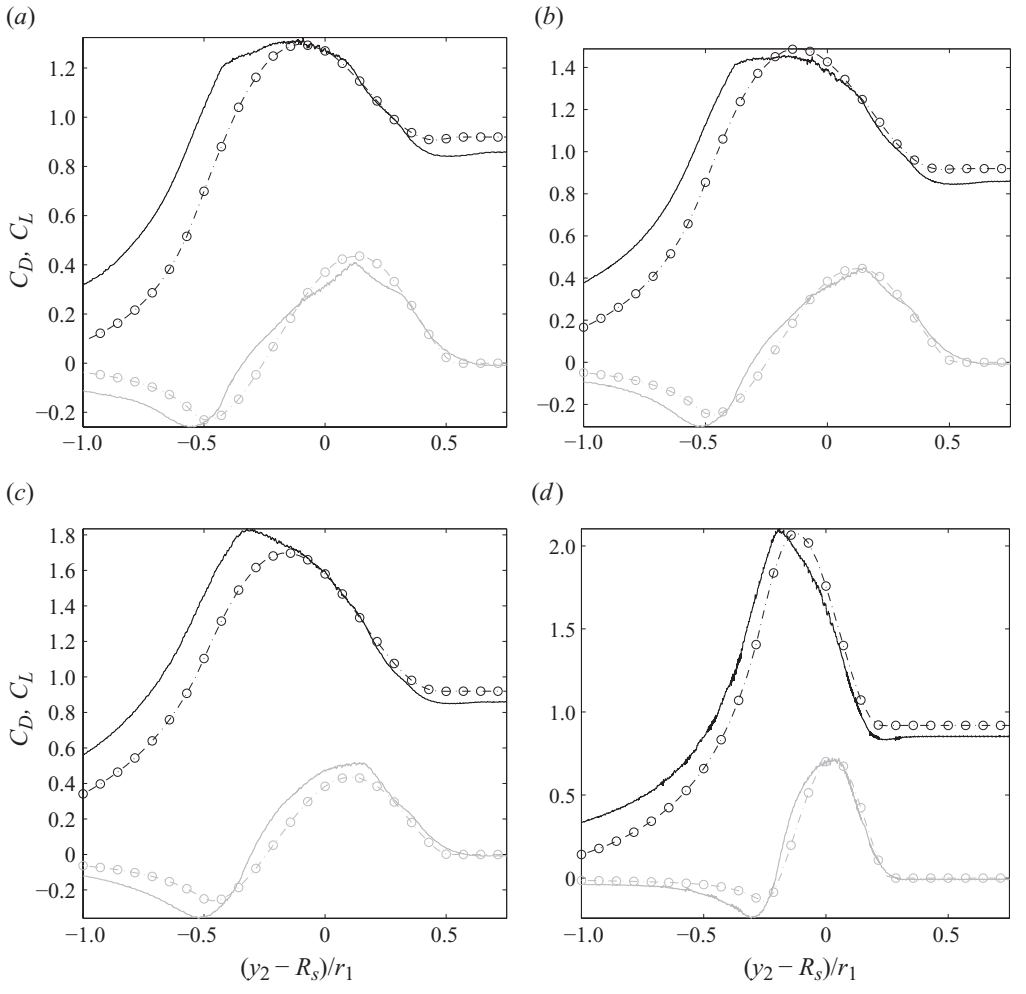


FIGURE 15. Interacting drag (dark) and lift (light) coefficients as functions of the normalised secondary lateral displacement for impulsively started two-sphere simulations at $M = 25$: (*a*) $r_2/r_1 = 0.5$, $\hat{x} = (x_2 - x_1)/r_1 = 1.5$; (*b*) $r_2/r_1 = 0.5$, $\hat{x} = 3.0$; (*c*) $r_2/r_1 = 0.5$, $\hat{x} = 8.0$; (*d*) $r_2/r_1 = 0.25$, $\hat{x} = 3.0$; —, computation; –·–○–·–, theory.

of the lift to the drag is well captured. Once some separation between the bodies has developed, the analytical model performs as indicated in figure 15.

Final computed separation velocities for the complete set of free-flying simulations are compared with the corresponding analytical values in figure 18. The normalised velocity $V_T' = \sqrt{\rho_m/\rho_a} V_T/V$, equal to $\sqrt{C}$ in (1.2), is plotted separately against the radius ratio for each of the Mach numbers investigated. As r_2/r_1 is decreased from 1, the computational profiles are seen to rise increasingly steeply until the critical radius ratio of approximately 0.45 is reached, at which point V_T' drops sharply. This drop indicates a transition from expulsion of the secondary body to entrainment within the region downstream of the primary shock (note that, as the separation velocity is not well-defined for entrainment, the value of V_T' plotted in this case corresponds to the maximum lateral velocity reached by the secondary body). Although it is not clear from figure 18, a marginally smaller critical r_2/r_1 occurs for $M = 25$, in part

https://doi.org/10.1017/jfm.2011.57 Published online by Cambridge University Press

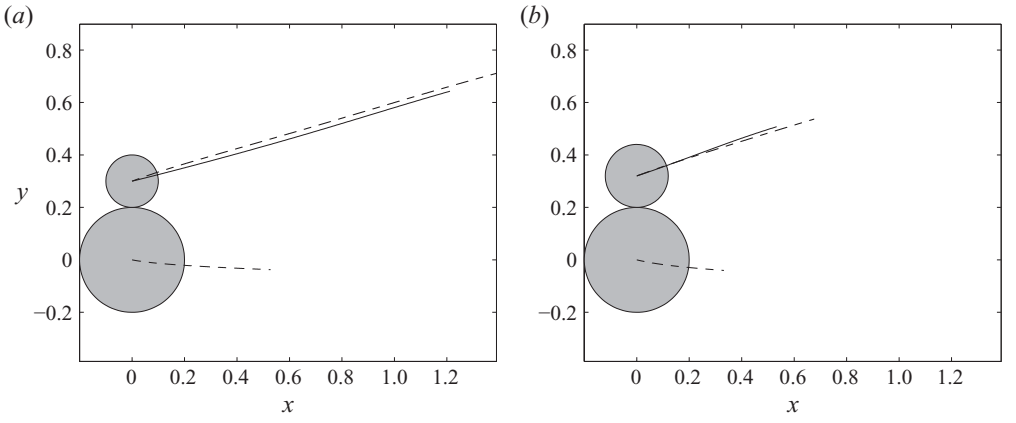


FIGURE 16. Computational (dashed) and analytical (solid) separation trajectories for radius ratios of $r_2/r_1 = 0.5$ (a) and 0.6 (b), at a Mach number of $M = 25$. Both trajectories are calculated until the analytical secondary body leaves the primary shock.

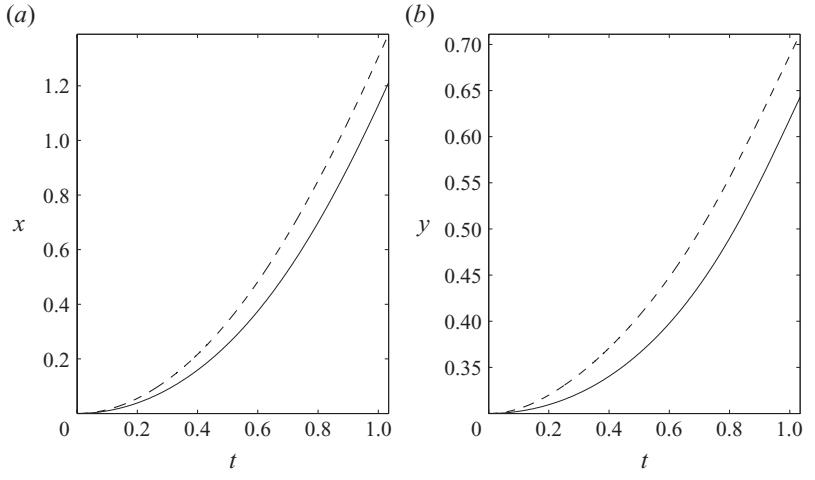


FIGURE 17. (a, b) Computational (dashed) and analytical (solid) secondary body displacements for $r_2/r_1 = 0.5$ and $M = 25$ (corresponding to the trajectory in figure 16a.)

due to the slight decrease in the radial location of the primary shock and in part due to the stronger bow-shock producing a larger secondary lift coefficient at the higher Mach number. The shift from expulsion to entrainment may be explained as follows. For larger secondary diameters ($r_2/r_1 \approx 1$), the secondary body initially exerts a significant repulsive force on the primary body (see § 4.6), and the separation is essentially a mutual repulsion. As the secondary size is decreased, however, the force on the primary body drops and the separation process becomes dominated by the secondary body's motion. As this happens, the effective initial lateral displacement of the secondary body also decreases, meaning that the L/D required for expulsion increases. Below the critical radius ratio, the L/D in the initial stages of motion is below this required value and entrainment results.

The analytical separation velocities show good agreement with computations at the maximum radius ratio of $r_2/r_1 = 1$ (which must be considered somewhat fortuitous),

https://doi.org/10.1017/jfm.2011.57 Published online by Cambridge University Press

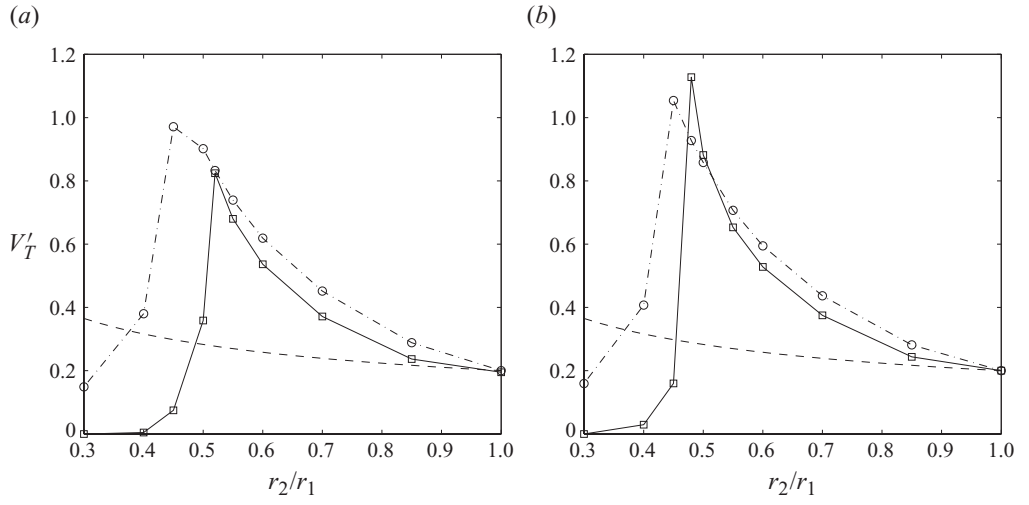


FIGURE 18. Normalised separation velocities, $V_T' = \sqrt{\rho_m/\rho_a}V_T/V$, for two initially touching spheres with centres axially aligned, for Mach numbers of 10 (*a*) and 25 (*b*): —□—, theory; –·–○–·–, numerical simulations; – – –, scaling indicated by (1.1). Note that for $M = 10$, $r_2/r_1 = 0.45$, the secondary body was still interacting with the primary bow-shock when it left the computational domain.

but then rise more gradually as the radius ratio is decreased. This is consistent with the comparative deficit in the analytical lift observed in the initial stages of the separation, as exemplified in figure 17. Slightly higher critical radius ratios, of 0.52 and 0.48, respectively, for $M = 10$ and 25, are predicted by the model than those observed in computations. Also, as r_2/r_1 decreases below this critical value, the analytical model predicts the maximum lateral velocity to drop more rapidly. Agreement for the higher Mach number of the two is superior; this is to be expected, as the blast-wave approximation assumes $M \to \infty$. According to (1.1), the normalised velocity plotted should scale as $\sqrt{r_1/r_2}$, and such curves are also shown in figure 18. This scaling is seen to give a poor approximation to the separation behaviour, however, and clearly does not predict a critical radius ratio that delineates entrainment from expulsion.

We conclude from these comparisons that the analytical model developed here, while limited in its ability to predict the forces accurately when the separation between the two bodies is small, provides satisfactory predictive ability elsewhere. In particular, it gives an adequate approximation to the secondary body trajectory and to the final separation velocity in simulating the separation of spherical fragments, especially at the Mach numbers relevant to meteoroid fragmentation (i.e. $M = 25$ and higher).

In the following two subsections, the analytical model is employed to further investigate the effects of varying the radius ratio, the initial positions and the relative initial velocities of the spheres. To avoid relying on the results of numerical simulations, the correlation of Billig (1967) is now used in place of a computational profile for the primary bow-shock shape. Also, the primary sphere motion is assumed to be unaffected by the presence of the secondary sphere, i.e. constant values of the primary drag and lift coefficients of $C_{D1} = 0.9$ and $C_{L1} = 0$ are assigned. For initially separated spheres, this is a reasonable assumption. For initially touching spheres, the influence of the secondary sphere on the primary drag in the free-flying

https://doi.org/10.1017/jfm.2011.57 Published online by Cambridge University Press

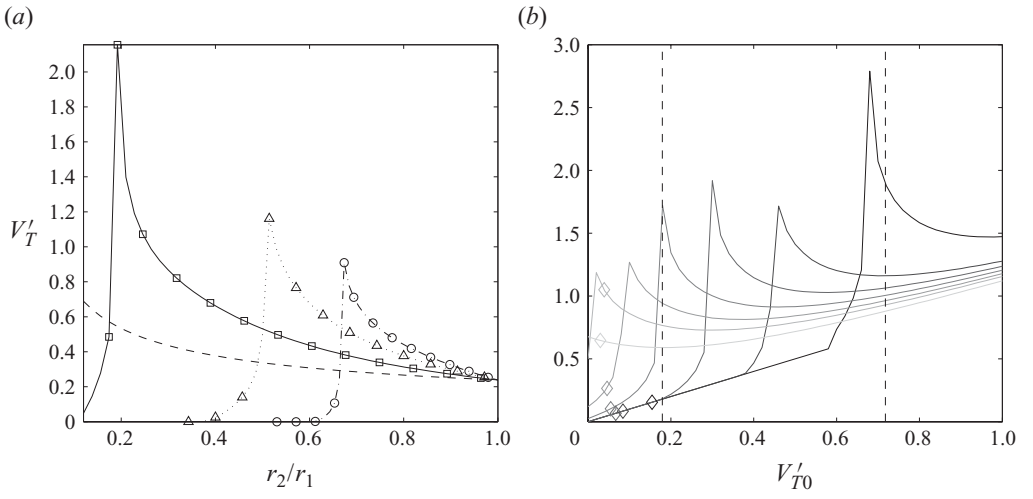


FIGURE 19. Normalised separation velocities calculated for initially touching spheres at a Mach number of $M = 25$, calculated using the analytical model. (*a*) Zero initial separation velocity with: –·–○–·–, rearmost points aligned; ···△···, centres aligned; —□—, frontmost points aligned; – – –, scaling indicated by (1.1). (*b*) Non-zero initial lateral velocities with sphere centres axially aligned, for (darkest to lightest): $r_2/r_1 = 0.2$, 0.3, 0.35, 0.4, 0.45, 0.5 and 0.6; ◇, maximum separation velocity from strain-energy conversion for the Sikhote-Alin meteoroid, according to (4.3). The vertical dashed lines indicate the maximum initial velocity from a spinning parent body, with parameters appropriate for the Sikhote-Alin meteoroid, assuming rotation rates of 1 and 4 r.p.s.

computations was found to be generally small ($\lesssim$13 % for $r_2/r_1 \lesssim 0.7$); thus, the assumption of zero lift here is approximately equivalent to modelling a symmetric three-body configuration with two secondary bodies. The differences between this and the original two-body configuration are described shortly. All calculations described in these subsections, unless stated otherwise, employ a Mach number of 25.

4.4. *Separation of spherical fragments*

In this subsection, we apply the analytical model to further arrangements in which the bodies initially touch to examine the effects of varying the initial point of alignment and the relative velocities of the bodies. With regard to the meteoroid fragmentation problem, this will give some indication of the influence that the disruption location within the parent body has on the subsequent separation behaviour, and the effects of combining aerodynamic interactions with other mechanisms that can influence the initial separation, such as parent-body rotation.

In figure 19(*a*), the final (or maximum, for entrainment) normalised separation velocity is plotted against the radius ratio for different choices of the axial alignment point of the spheres: alignments of the centres (as before), of the frontmost point and of the rearmost point are considered (see figure 3*c*; the three of course coincide for $r_2 = r_1$). The initial relative velocity is zero in all cases. First, by comparing the centre-aligned profile with the analytical $M = 25$ profile in figure 18, the influence of neglecting the repulsive effect of the secondary body on the primary body (i.e. assigning $C_{L1} = 0$) can be deduced. The critical radius ratio is shifted to a slightly higher value, 0.51 compared with 0.48, and, if expelled, the secondary separation velocity is augmented by a small amount. Comparing the profiles for the three alignment points, the critical radius ratio increases from 0.19 for front alignment to

https://doi.org/10.1017/jfm.2011.57 Published online by Cambridge University Press

0.51 for centre alignment, through to 0.67 for rear alignment. This can be explained by the increase in the effective radial shock location experienced by the secondary body as it is moved from the front to the rear. The maximum separation velocity also increases as the critical radius ratio decreases, since smaller bodies experience larger accelerations. Note that the scaling of Passey & Melosh (1980) equation (1.1) gives a result closest to the front-aligned profile, since the assumption of a purely lateral separation is most appropriate in this case.

We now consider the separation behaviour when there is a non-zero initial relative velocity between the fragments, V'_{T0}. This initial velocity may result, for example, from rotation of the parent body (Passey & Melosh 1980) or from conversion of the strain energy in the parent body prior to disruption into kinetic energy of the fragments. A rough upper bound for the velocity produced by the latter mechanism can be estimated as follows. The potential strain energy in a body undergoing uniaxial compression is approximately $\varepsilon_s = \bar{p}^2 Al/(2E) = \bar{p}^2 m_0/(2\rho_m E)$, where A, l and m_0 are respectively the frontal area, length and mass of the body, $\bar{p}$ is the mean pressure, and E is the Young's modulus. If this energy is assumed to be converted entirely into lateral kinetic energy of the fragment pair, conservation of momentum gives $(1 + m_2/m_1)m_2 V_T^2 = 2\varepsilon_s$. Using $m_0/m_2 = 1 + m_1/m_2$, we then obtain

$$\frac{V_{T0,max}}{V} = \left(\frac{1}{\rho_m E} \frac{1 + (r_1/r_2)^3}{1 + (r_2/r_1)^3} \right)^{1/2} \rho_a V. \tag{4.3}$$

The maximum separation velocity from this mechanism thus increases approximately as $(r_2/r_1)^{-3/2}$ as r_2/r_1 is decreased.

If both the magnitude and the direction of the initial separation velocity are allowed to vary, as well as the initial alignment of the fragments, the parameter space becomes too large to fully investigate. We thus limit ourselves to purely lateral initial separation velocities and axial alignment of the sphere centres (figure 3*d*). In figure 19(*b*) is plotted the final (or maximum, for entrainment) normalised separation velocity versus the initial normalised velocity, $V'_{T0} = \sqrt{\rho_m/\rho_a} V_{T0}/V$, for a number of choices of r_2/r_1. As V'_{T0} is increased, extended surfing becomes possible for smaller radius ratios, leading to a decreased critical r_2/r_1. This is similar to the effect of moving the alignment point forward, as discussed earlier; the corresponding increase in the maximum separation velocity is also generally observed (note, however, that the precise value of the maximum for a given r_2/r_1 is sensitive to the choice of initial conditions, so the peak in each profile should be considered a lower bound). On each of the curves is also indicated the point corresponding to the maximum initial separation velocity available from strain-energy conversion for that radius ratio (4.3) for parameters appropriate for the Sikhote-Alin meteoroid at break-up (Krinov 1966). Since this meteoroid underwent multiple stages of fragmentation, the height of the second-to-last stage according to eyewitness accounts (16 km), which was most likely responsible for the major dimensions of the crater field, is chosen, giving an atmospheric density of $\rho_a = 0.17\,\mathrm{kg\,m^{-3}}$. The values of the other parameters are $V = 15\,\mathrm{km\,s^{-1}}$ and $E = 200\,\mathrm{GPa}$. Strain-energy conversion is seen to have only a limited potential effect on the separation behaviour: even for this limiting case, the critical radius ratio drops by only a small amount to slightly below 0.5. For weaker bodies (e.g. stones), the reduced E in (4.3) will be offset by a decreased ρ_a at the point of disruption, and these results will not be substantially altered.

Figure 19(*b*) also shows vertical lines corresponding to the maximum initial separation velocities resulting from rotation rates of $\omega_0 = 1$ and 4 r.p.s. for the

https://doi.org/10.1017/jfm.2011.57 Published online by Cambridge University Press

Sikhote-Alin parent body. These assume an initial mass of 300 tonnes (Heide 1963), and thus, with a density of $\rho_m = 7800\,\mathrm{kg\,m^{-3}}$, a radius of approximately 2 m. The effect of spinning on the subsequent surfing behaviour is seen to be potentially much more significant for meteoroids of this size than strain-energy conversion: for 1 and 4 r.p.s., the critical radius ratio drops to 0.4 and ~0.2, respectively. Moving the initial point of alignment forward, or increasing the parent body radius, would decrease the critical ratio even further. These results also show that the combined effects of surfing and a modest rotation rate give the potential for a significant variation in the final separation velocity. The maximum separation velocity for $r_2/r_1 = 0.2$ in figure 19(*b*) corresponds to a value of $C = 1.56$ in (1.1); thus, a large fraction of the variation deduced in this 'constant' by Passey & Melosh (1980) from terrestrial crater fields (see § 1) can be explained by the combination of these two mechanisms.

4.5. *System dynamics in sphere–sphere surfing*

We now investigate the effect of varying the initial lateral separation of the spheres (figure 3*e*), in particular to determine whether a range of stable surfing behaviour, as was found for the sphere-wedge arrangement, can be established. For the initially touching two-sphere configurations considered thus far, surfing was found in general to be unstable. This is because for a secondary body sufficiently large to avoid entrainment, the lateral momentum developed during the interaction phase is typically high enough that, as the secondary body exits the influence of the primary shock, the flow cannot bend its trajectory around more quickly than the rate of decrease in the shock angle. By varying the initial lateral separation, however, the initial repulsion for large secondary bodies can be decreased; also, surfing becomes possible for smaller radius ratios. It will thus prove possible to reproduce surfing behaviour similar to that observed in the sphere-wedge configuration.

4.5.1. *Sphere trajectories*

In figure 20 are plotted secondary body trajectories for four different choices of radius ratio: $r_2/r_1 = 0.05$, 0.1, 0.2 and 0.5, each with four choices of the initial lateral position (relative to the shock). These are obtained by integrating (3.4) for each of the two spheres. For the primary body, having already assumed the force coefficients to be constant, the integration is trivial. For the secondary body, now $\hat{x} = (x_2 - x_1)/r_1$ and $\hat{y} = (y_2 - y_1)/r_1$ in the evaluation of C_D and C_L. In all cases shown, the secondary and primary body centres are initially aligned in the axial direction and the initial velocities are zero. The abscissa in each plot is the normalised axial distance between the sphere centres, $\hat{x}$; the ordinate is the lateral distance between the secondary centre and the radial shock location, R_s, normalised by the secondary radius. Thus, the secondary body is completely outside the flow region downstream of the primary shock for $(y_2 - R_s)/r_2 > 1/\cos\beta$. This scaling was chosen as it is the most convenient for the following analysis.

For all r_2/r_1, the minimum initial separation considered of $y_{20} - R_s = 0$ (at which the initial lateral force is close to a maximum) results in the secondary body being quickly ejected from the region behind the primary bow-shock. For the two smaller r_2/r_1, the aerodynamic forces acting in the undisturbed free stream are sufficient to turn the trajectory so that the secondary body re-enters this region, only for it to be ejected once again (for $r_2/r_1 = 0.05$, a further re-entry occurs at $\hat{x} \approx 20$). For the two larger radius ratios, the secondary body remains outside after the first ejection. For the maximum initial separation shown, $(y_{20} - R_s)/r_2 = 1.5$, the secondary

https://doi.org/10.1017/jfm.2011.57 Published online by Cambridge University Press

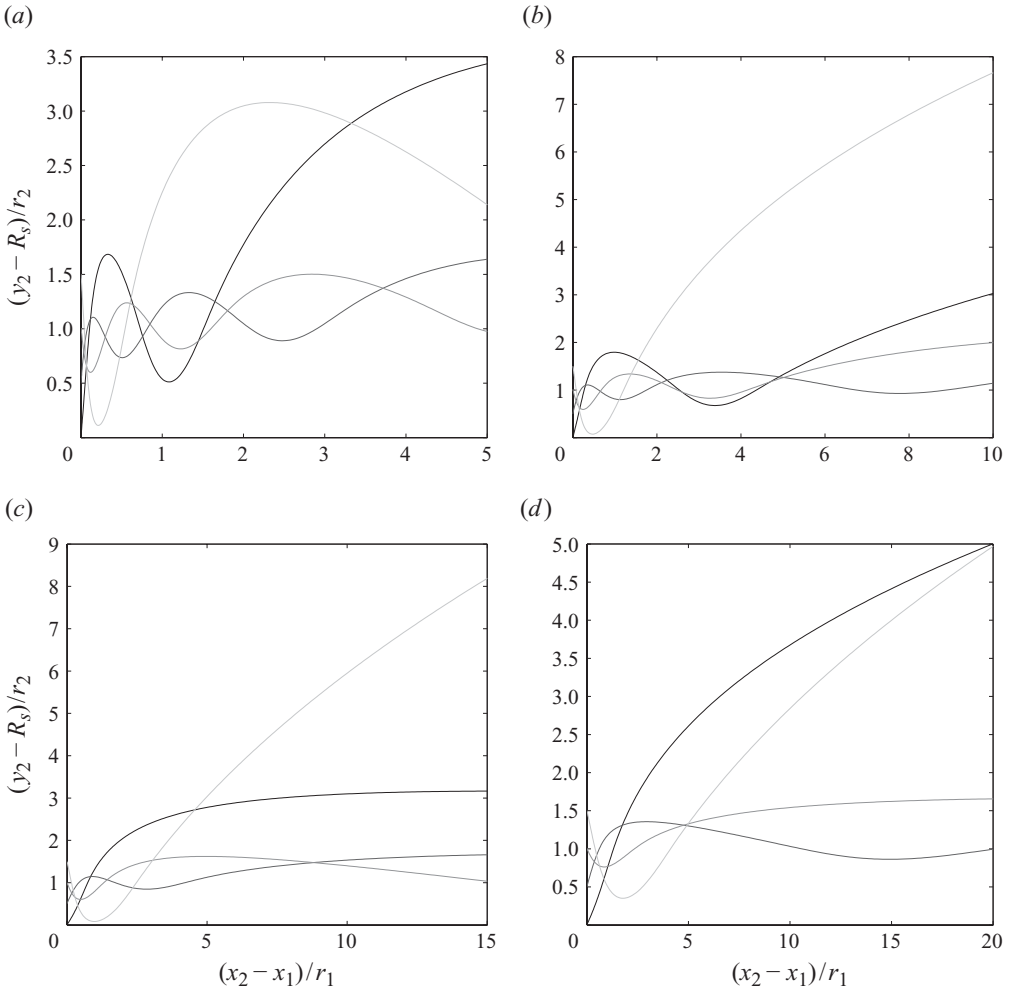


FIGURE 20. Theoretical secondary trajectories in normalised coordinates for various initial lateral positions, for radius ratios of $r_2/r_1 = 0.05$ (*a*), 0.1 (*b*), 0.2 (*c*), and 0.5 (*d*), all at Mach 25. Note the differences in horizontal and vertical scales.

bodies begin their trajectories outside the influence of the primary shock. The axial momentum developed in the free stream allows the body to penetrate deep into the flow region downstream of the shock in each case, but the large repulsive forces then encountered cause it to be strongly expelled. Increasing the initial separation further to $(y_{20} - R_s)/r_2 = 2$ (not shown) results in the secondary body penetrating completely inside this region and becoming entrained for all but the largest radius ratio. For the two intermediate initial separations, $(y_{20} - R_s)/r_2 = 0.5$ and 1.0, the secondary body motion is similar to the oscillatory behaviour observed for sphere-wedge interactions, with the sphere dipping in and out of the region behind the primary shock, but typically failing to develop sufficient lateral momentum to be decisively ejected. The oscillation wavelength increases with r_2/r_1, and, because of the decreasing shock angle with $\hat{x}$, does so more rapidly than according to the linear relationship that is exhibited for a planar shock. It should be noted that such oscillating trajectories can also result

https://doi.org/10.1017/jfm.2011.57 Published online by Cambridge University Press

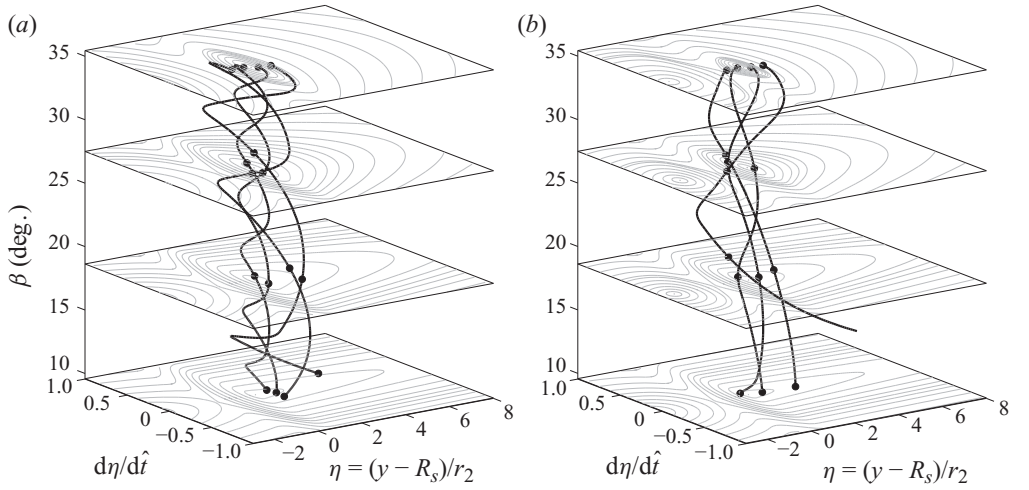


FIGURE 21. Secondary body trajectories in the phase space at Mach 25, corresponding to the normalised trajectories in figure 20: $r_2/r_1 = 0.05$ (*a*) and 0.2 (*b*). The local phase planes are at cuts of $(x_2 - x_1)/r_1 = 0$, 1, 4 and 20; the markers indicate the points at which the trajectories cross each of the phase planes.

for smaller secondary bodies ($r_2/r_1 \lesssim 0.1$) in initially touching configurations, if they are given a sufficiently large initial lateral velocity.

4.5.2. *Phase-space behaviour*

It is clear from the trajectories just discussed that the sphere–sphere system behaviour is at least, to some extent, similar to that of the sphere-wedge configuration. Unfortunately, now that the shock angle β is a function of $\hat{x}$, the flow similarity that enabled (3.4) to be reduced to (3.5) no longer exists. However, by introducing a third equation for β in addition to those for η and v_η, a phase-space analysis is made possible. The governing equations are given and discussed in the Appendix: other than the introduction of the additional equation, the key differences between this set of equations and (3.5) are in the equation for v_η; namely, the replacement of the single sphere drag coefficient, C_D, with $C_{D2} - C_{D1}$, and the introduction of a shock-curvature term involving $\mathrm{d}\beta/\mathrm{d}\hat{t}$ (where $\hat{t} = \sqrt{\rho_a/\rho_m}\, tV/r_2$) and the relative axial velocity, $\hat{v}_{x2} - \hat{v}_{x1}$. Both of these factors serve to augment the effective lift/drag ratio of the secondary body.

In figure 21 are plotted the phase-space counterparts of the physical trajectories in figure 20 for two radius ratios, $r_2/r_1 = 0.05$ and 0.2. In addition, local phase planes of η and v_η are shown for values of β corresponding to $\hat{x} = 0$, 1, 4 and 20. These are obtained by approximating the shock-curvature term as independent of the initial value of η (see the Appendix). The general features of these phase planes are, in part, similar to those of the sphere-wedge phase diagram in figure 11, with the two stationary points present in all cases. For both radius ratios, however, the stable region in the phase plane is seen to expand considerably in the downstream direction, and this is mirrored in the growing amplitudes of the trajectory oscillations (perhaps seen more clearly in figure 20). This may be attributed to the augmentation of the effective L/D ratio referred to in the previous paragraph. The growth of the stable region also means that the $r_2/r_1 = 0.2$, $(y_{20} - R_s)/r_2 = 1.5$ trajectory, though beginning slightly outside the local stable region, is nevertheless not entrained. In spite of this growth,

https://doi.org/10.1017/jfm.2011.57 Published online by Cambridge University Press

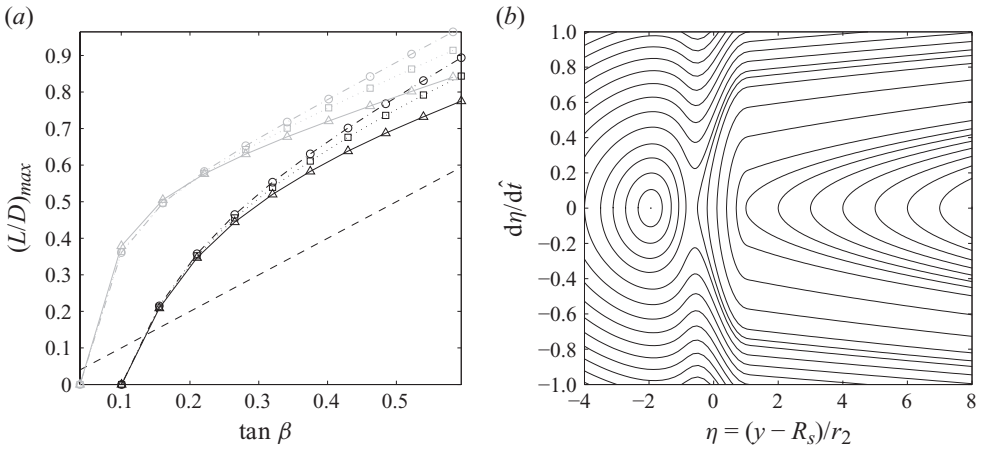


FIGURE 22. (*a*) Maximum lift-to-drag ratios for the secondary sphere at $M=10$ (dark) and $M=25$ (*b*): $-\cdot-\bigcirc-\cdot-$, $r_2/r_1=0.1$; —△—, $r_2/r_1=0.2$; $\cdots\square\cdots$, $r_2/r_1=0.5$; $--$, $(L/D)_{max}=\tan\beta$. (*b*) Phase plane showing the disappearance of the principal stable region.

the positions of the stationary points vary but very little downstream: for $r_2/r_1=0.05$, the stable point, for example, shifts from $\eta=0.76$ at $\hat{x}=0$ to 0.95 at $\hat{x}=20$; for $r_2/r_1=0.2$, the variation is from 0.73 to 0.96. The most notable differences between the pictures for the two radius ratios are the smaller region of stability in the phase plane (most apparent upstream), and the reduced number of trajectory oscillations, for the larger r_2/r_1. The latter point is obvious from dimensional considerations; the former is discussed shortly.

A significant difference between the present phase diagrams and those of sphere-wedge configurations is the presence of a second stationary point – another centre – at $\eta<0$ (for clarity, we now refer to the first centre and its bounding stable region as 'principal'). This may be a result of the approximations inherent in the analytical model, however, and is discussed in the Appendix.

Phase-space pictures corresponding to those in figure 21 were also obtained for $M=10$. The main features of the local phase planes are generally similar, but the principal stable regions are initially slightly smaller for the lower Mach number, and, after reaching a maximum extent near $\hat{x}=4$, begin shrinking in the downstream direction; the oscillations in the secondary trajectories show corresponding reductions in amplitude downstream. One might suspect that these differences are related to the Mach number effect observed in figure 8(*b*), as it is reasonable to assume that the extent of the principal stable region in the local phase plane will be determined by the degree to which the maximum L/D value exceeds $\tan\beta$. To test this, in figure 22(*a*), $(L/D)_{max}$ is plotted against $\tan\beta$ for Mach numbers of 10 and 25 and for various radius ratios. Here $L/D=[C_{L2}-(r_2/r_1)C_{L1}]/[C_{D2}-(r_2/r_1)C_{D1}]$ and thus is strictly only the effective lift/drag ratio when the shock-curvature term is zero. However, the shock-curvature term varies but very little between these two Mach numbers, so plotting in this form better highlights the differences between the two. The line $(L/D)_{max}=\tan\beta$ is included for reference, but the location where each curve intersects this line now has little physical significance. As in the sphere-wedge case, $(L/D)_{max}$ initially lies well above $\tan\beta$ for both Mach numbers and for all radius ratios. As β is decreased, however, the $M=10$ profiles drop more steeply, whereas the $M=25$ curves remain well above the $\tan\beta$ line over a large range of β,

https://doi.org/10.1017/jfm.2011.57 Published online by Cambridge University Press

with the ratio $(L/D)_{max}/\tan\beta$ increasing until $\tan\beta \approx 0.15$. This provides a holistic explanation as to why the size of the principal stable region begins to decrease in the downstream direction in the $M = 10$ phase diagrams but continues to increase for $M = 25$. If the Mach number is decreased further, the size of the stable region should continue to shrink; unfortunately, the use of the blast-wave analogy means that the analytical model cannot be expected to give reliable results for Mach numbers much below 10.

A further observation from figure 22(*b*) is that, for a given Mach number and β, $(L/D)_{max}$ is minimum for $r_2/r_1 \approx 0.2$. This explains the decreased extent of the principal stable regions for this radius ratio compared to $r_2/r_1 = 0.05$ in figure 21. The reason for this effect is that, as r_2/r_1 is increased, though the peak C_{L2} decreases monotonically, the influence of the $r_2/r_1 \times C_{D1}$ term in the denominator of L/D becomes increasingly dominant.

As noted earlier, the effect of the augmentation of the effective L/D ratio by the shock-curvature term is to enlarge the principal stable region; however, if this augmentation is sufficiently large, the principal stable region can disappear altogether (this is equivalent to lifting the L/D profile in figure 8*a* such that the free-stream value lies above the horizontal $\tan\beta$ line). An example of such a phenomenon is shown in figure 22(*b*); a further discussion appears in the Appendix.

Finally, we are now in a position to predict the phase-plane picture for initial conditions other than $\hat{x}(0) = 0$ and $\hat{v}_{x2}(0) - \hat{v}_{x1}(0) = 0$, as assumed thus far. For $\hat{x}(0) < 0$ or $\hat{v}_{x2}(0) - \hat{v}_{x1}(0) \neq 0$, the magnitude of the shock-curvature term will increase for a given β, enlarging the principal stable region or transforming the phase plane into the form seen in figure 22. Conversely, for $\hat{x}(0) > 0$, the shock-curvature term will become smaller, shrinking the principal region of stability. Even as this term tends to zero, however, the principal stable region will remain finitely large except for β only slightly greater than the Mach angle. This may be deduced from figure 22(*a*), in which the intersections of the $(L/D)_{max}$ curves with the $\tan\beta$ line give the minimum β for the existence of a stable region in this limit.

4.6. *Primary body motion for initially touching configurations*

In previous separate fragment models (Artemieva & Shuvalov 2001; Bland & Artemieva 2006), the separation behaviour of the primary body was derived from conservation of lateral momentum applied to the fragment pair. This assumption, while valid for equally sized fragments (but from symmetry rather than mechanical considerations), was proposed by the authors with some doubts as to its validity when $r_2 \neq r_1$. Indeed, both the presence of intervening fluid (to which momentum may be transferred) and the limited domain of influence of a body in supersonic flow may lead one to question this assumption, even without knowledge of the surfing phenomenon. With the highly asymmetrical domains of influence produced by surfing, however, it is clearly not appropriate to correlate the final lateral momenta of the two bodies. In the computations described in § 4.3, for example, the magnitude of the maximum lateral momentum of the secondary body varies from less than a third to more than twice that of the primary body.

The analytical model developed in this work does not tell us anything about the motion of the primary body during separation from an initially touching configuration, and to obtain quantitative results we must look to the relevant computations. These can still be informed by general physical arguments, however. Following a line of

https://doi.org/10.1017/jfm.2011.57 Published online by Cambridge University Press

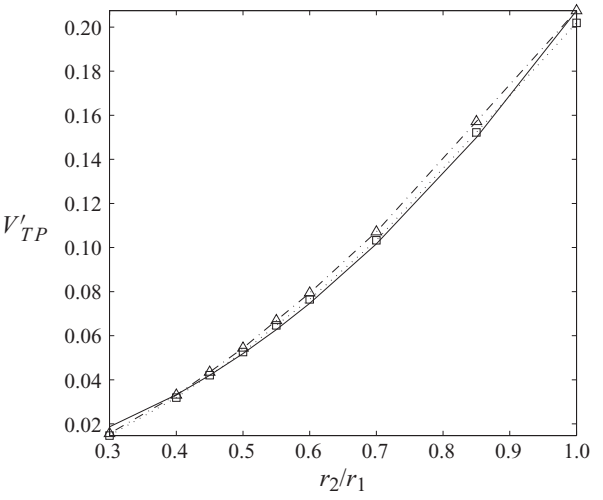


FIGURE 23. Normalised separation velocity of the primary body from numerical simulations of initially touching two-sphere configurations: $-\cdot-\triangle-\cdot-$, $M=10$; $\cdots\square\cdots$, $M=25$; ——, $V'_{TP} \propto (r_2/r_1)^2$.

reasoning similar to Passey & Melosh (1980), we write

$$V_{TP} = \bar{F}_{TP}\Delta t/m_1, \tag{4.4}$$

where V_{TP} is the final separation velocity of the primary body, $\bar{F}_{TP}$ is the mean lateral force, and Δt is the time period over which the secondary body influences the primary body. Assuming the separation to be dominated by the secondary body's motion, we may characterise the influence time as $\Delta t = \sqrt{2\xi/\alpha_2}$, where ξ and α_2 are the secondary body's influence distance and separation acceleration, respectively. The influence distance will scale as $\xi \propto r_2^k$, where $0 \lesssim k \lesssim 1$: the upper limit for k is appropriate for $r_2 \approx r_1$, in which case the separation is principally lateral and the influence distance scales with the radial location of the secondary shock; for $r_2 \ll r_1$, however, the separation is principally axial due to the significantly higher axial acceleration of the secondary body, and the dependence of ξ on r_2 will be weak. In either case, the secondary acceleration will scale roughly as $\alpha_2 \propto 1/r_2$. The lateral force exerted by the secondary body on the primary body, $\bar{F}_{TP}$, will also depend on the secondary size, as a larger secondary body will have a larger pressure footprint on the primary surface. If the primary surface were planar, this would result in $\bar{F}_{TP} \propto r_2^2$ (which will be the limiting behaviour as $r_2/r_1 \to 0$), but, because of the curvature of the primary surface, the dependence will, in general, be less than quadratic.

Combining these dependencies, we have $V_{TP} \propto r_2^m$, where $1 \leqslant m \leqslant 3$, and with $m \approx 2$ likely to be an appropriate value over a range of r_2/r_1. Indeed, in figure 23, the normalised primary separation velocities from the free-flying simulations described in § 4.3 are plotted, and a value of $m=2$ in the scaling of V_{TP} is seen to provide a good fit to the data. Although these arguments are not sufficient in themselves to provide quantitative information regarding the primary separation behaviour, with a small number of relevant computations, they can be used to extrapolate the primary body's behaviour over a range of relative body sizes.

https://doi.org/10.1017/jfm.2011.57 Published online by Cambridge University Press

5. Discussion

We conclude with a brief discussion of the implications of the shock-surfing phenomenon, particularly for meteoroid fragmentation. First, because of the dependence of the extent of surfing on the radius ratio in initially touching configurations, and the highly augmented separation velocities that can result from extended surfing, it is clear that the radius ratio is a critical parameter in determining the separation behaviour. The influence of the radius ratio is not captured well by the scaling law of Passey & Melosh (2008) equation (1.1) and moreover, the extrapolation of the separation behaviour of equally sized fragments to unequal fragments, as in previous separate fragment models (Artemieva & Shuvalov 2001; Bland & Artemieva 2006), is unlikely to yield accurate results. The implications of surfing for the assumption of conserved lateral momentum in deriving the primary motion in these models have also been discussed.

The existence of a critical radius ratio (or, more correctly, a critical ratio range, given that a number of factors affect the precise value of this ratio), delineating entrainment of the secondary body within the region bounded by the primary bow-shock from expulsion, will also lead to a selection effect for multiple fragments travelling together, for instance immediately following atmospheric disruption of the parent body. The largest fragments will repulse one another, but with moderate resulting separation velocities; slightly smaller fragments will have the potential to be repulsed strongly due to surfing effects, whereas the smallest fragments are likely to be entrained by larger fragments (at which point a further selection effect can take place due to the dependence of the lateral force coefficient on the radius ratio noted by Laurence *et al.* 2007). This could lead to interesting and observable phenomena in the formation of crater fields: for example, outlying fragments could be produced by extended surfing immediately following disruption, and smaller fragments could impact further downrange than would otherwise be possible due to their travelling within the low-density region behind larger fragments. Regarding this last point, one of the 'peculiarities' of the Sikhote-Alin crater field noted by Krinov (1966) is that 'a fairly large number of small craters and holes were found to lie in the front part between large craters'. This may in fact not be a peculiarity at all, but an expected result of interactions between fragments of different sizes.

Finally, the shock interactions experienced during surfing will lead to extremely high local pressures and heat fluxes on the surfing body (Edney 1968; Sanderson, Hornung & Sturtevant 2004). Such interactions, for example, were responsible for burning 'gaping holes' in the pylon of a dummy ramjet attached to the X-15 aircraft (Bertin & Cummings 2006). This increased dynamic and thermal loading would lead to enhanced ablation and possibly further fragmentation of the affected fragment, and would also increase the rate of energy transfer to the atmosphere.

S.J.L. was a postdoctoral scholar at the Graduate Aeronautical Laboratories, California Institute of Technology, under the supervision of Professor H. Hornung, when this work began, and is grateful for many fruitful discussions with Professor Hornung on the subject. S.J.L. also acknowledges H. J. Melosh, whose critique of an earlier work helped lead to the present manuscript. The large-scale parallel computations were carried out using resources of the Oak Ridge Leadership Computing Facility at Oak Ridge National Laboratory, which is supported by the Office of Science of the Department of Energy under contract DE-AC05-00OR22725.

https://doi.org/10.1017/jfm.2011.57 Published online by Cambridge University Press

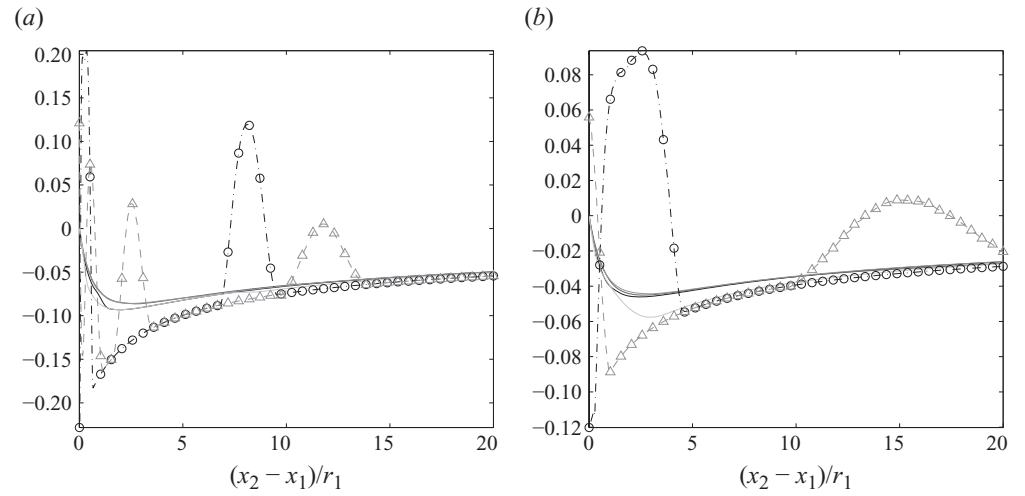


FIGURE 24. Terms in (A 1*b*) for the $r_2/r_1 = 0.05$ (*a*) and 0.5 (*b*) trajectories shown in figure 20: (solid) shock-curvature term for $(y_{20} - R_s)/r_2 = 0$, 0.5, 1.0 and 1.5 (dark to light); (symbols) force-coefficient term for $(y_{20} - R_s)/r_2 = 0.5$ (−−△−−) and 1.5 (−·−○−·−).

Appendix. Governing equations for sphere–sphere dynamics in phase space

To derive the equivalent set of equations to (3.5) for sphere–sphere dynamics, we begin by assuming that the Mach number and radius ratio are given, and that the spheres are initially stationary. In analogy with the reasoning that led to (3.5), we now write $\eta = (y_2 - R_s)/r_2$, so that $v_\eta = \mathrm{d}\eta/\mathrm{d}\hat{t} = \hat{v}_{y2} - \hat{v}_{y1} - \tan\beta\,(\hat{v}_{x2} - \hat{v}_{x1})$, where $\hat{t} = \sqrt{\rho_a/\rho_m}\,tV/r_2$. The analogous system of equations to (3.5) is then

$$\frac{\mathrm{d}\eta}{\mathrm{d}\hat{t}} = v_\eta, \tag{A 1a}$$

$$\frac{\mathrm{d}v_\eta}{\mathrm{d}\hat{t}} = \underbrace{\frac{3}{8}\left[C_{L2}(\beta,\eta) - \frac{r_2}{r_1}C_{L1} - \tan\beta\left(C_{D2}(\beta,\eta) - \frac{r_2}{r_1}C_{D1}\right)\right]}_{} - \underbrace{\frac{\hat{v}_{x2} - \hat{v}_{x1}}{\cos^2\beta}\frac{\mathrm{d}\beta}{\mathrm{d}\hat{t}}}_{}, \tag{A 1b}$$

$$\frac{\mathrm{d}\beta}{\mathrm{d}\hat{t}} = \frac{r_2}{r_1}(\hat{v}_{x2} - \hat{v}_{x1})\frac{\mathrm{d}\beta}{\mathrm{d}\hat{x}}, \tag{A 1c}$$

where any newly introduced notation has its obvious meaning. As discussed in § 4.3, C_{D1} and C_{L1} are assumed to be constant; in particular $C_{L1} = 0$. Since β is a single-valued function of $\hat{x}$, we can easily reverse this dependency and write $\hat{x} = \hat{x}(\beta)$. In this case, the derivative $\mathrm{d}\beta/\mathrm{d}\hat{x}$ in (A 1*c*) becomes $(\mathrm{d}\hat{x}/\mathrm{d}\beta)^{-1}$. However, (A 1*a–c*) is prevented from being an autonomous system for η, v_η and β by the appearance of $\hat{v}_{x2} - \hat{v}_{x1}$ in (A 1*b*) and (A 1*c*). In general, this expression, representing an integrated drag coefficient, depends on $\hat{t}$, $\eta(0)$ and $\beta(0)$. Note that it is also not reasonable to avoid this problem by simply neglecting the relevant term in (A 1*b*). To show this, in figure 24 are plotted the two underbracketed terms in (A 1*b*) (which we refer to as the force-coefficient and shock-curvature terms, respectively) versus $\hat{x}$ for the $r_2/r_1 = 0.05$ and 0.5 trajectories from figure 20. Except for the initial stages of the motion, the magnitudes of the two terms are seen to be comparable. However, if we limit ourselves to a single initial axial position, characterised by $\beta(0)$, the value of $\hat{v}_{x2} - \hat{v}_{x1}$ should vary but weakly with the initial lateral position, $\eta(0)$, and may then be approximated as a function only of β (or of $\hat{t}$, as the two are now equivalent). If

https://doi.org/10.1017/jfm.2011.57 Published online by Cambridge University Press

this approximation is reasonable, the shock-curvature term profiles in figure 24 should be roughly independent of y_{20}. For $r_2/r_1 = 0.05$, this is indeed true. For $r_2/r_1 = 0.5$, the single profile corresponding to $(y_{20} - R_s)/r_2 = 1.5$ diverges from the others, due to the high drag experienced by the secondary body as it penetrates deeply into the flow region downstream of the primary shock in this case. Overall, however, this approximation may be considered reasonable.

Therefore, (A 1) can now be treated as an autonomous system and, moreover, the right hand side of (A 1*c*) is a function only of β; thus, β can be solved for independently of η and v_η. This enables the construction of local phase planes of η and v_η for given values of β that can be used to elucidate the behaviour of the secondary trajectories in phase space; examples of such local phase planes are shown in figure 21. It is to be understood, however, that this description is only valid for the single considered value of the initial axial position, $\beta(0)$ (as well as of the initial axial velocity, $\hat{v}_{x2}(0) - \hat{v}_{x1}(0)$), and even so, only under the assumption that the shock-curvature term is independent of $\eta(0)$. To produce the local phase planes shown in figure 21, the mean value of the shock-curvature term over the four considered trajectories at each point downstream was used.

Comparing now (3.5) and (A 1), the key difference is the introduction in (A 1*b*) of the shock-curvature term, $(r_2/r_1)[(\hat{v}_{x2} - \hat{v}_{x1}/\cos\beta]^2 \mathrm{d}\beta/\mathrm{d}\hat{x}$. Physically, the influence of the shock curvature is to increase the effective magnitude of v_η as the secondary body moves away from the shock, but to decrease it as the body approaches the shock; thus, the presence of this term will enlarge the region of stability in the local phase plane. This may also be understood mathematically to arise from the fact that $\mathrm{d}\beta/\mathrm{d}\hat{x}$ is always negative, so the shock-curvature term will act as a positive contribution to the lift coefficient, decreasing the minimum value of C_{L2} for which a stable stationary point can exist. This effect is further augmented by the introduction of the primary drag coefficient, C_{D1}, in the force-coefficient term. However, if the combined effect is sufficiently large that $(r_2/r_1)[(\hat{v}_{x2} - \hat{v}_{x1})/\cos\beta]^2 |\mathrm{d}\beta/\mathrm{d}\hat{x}| > \tan\beta\,(1 - r_2/r_1)C_{D,fs}$, where $C_{D,fs}$ is the free-stream drag coefficient, then no stable stationary point will exist (this is equivalent to lifting the L/D profile in figure 8*a* such that the free-stream value lies above the horizontal $\tan\beta$ line). In this case, no stable surfing is possible; figure 22(*b*) shows that such a situation is realisable, at least locally. This phase plane is for $M = 25$, $r_2/r_1 = 0.2$ and $\hat{x} = 4$, but using the larger shock-curvature term corresponding to the $(y_{20} - R_s)/r_2 = 1.5$ trajectory, rather than the mean value over the four trajectories. The principal stable region is seen to disappear altogether, though the saddle point and the inner stable region remain. This behaviour helps to explain why the relevant trajectory in figures 20 and 21 shows such large amplitude oscillations. The rapid decay of the shock-curvature term downstream, however, means that the phase plane reverts to its more familiar appearance by $\hat{x} = 20$, and even this trajectory will eventually take the secondary body back towards the primary shock.

As mentioned in § 4.5.2, a significant difference between the sphere–sphere phase diagrams and those of sphere-wedge configurations is the presence of a second centre at $\eta < 0$. This centre is visible in the $r_2/r_1 = 0.2$ phase planes, but is also present in all those for $r_2/r_1 = 0.05$ (though outside the plotted limits) except for that corresponding to $\hat{x} = 0$. The appearance of this second stable point is due to the rapid drop in the value of C_{D2} as η decreases inside the region downstream of the primary shock (see figure 15), which means that the positive C_{D1} and shock-curvature terms in (A 1*b*) become dominant, and $\mathrm{d}v_\eta/\mathrm{d}\hat{t}$ switches sign from negative to positive. When this happens, the formerly open phase paths become closed circuits bounding the two stable regions, and it is possible for the secondary body to exhibit oscillations that

https://doi.org/10.1017/jfm.2011.57 Published online by Cambridge University Press

take it from fully inside to fully outside the flow region bounded by the primary shock and back again. These predictions should be treated with some caution, however: figure 15 shows that the analytical model predicts C_{D2} to drop more rapidly inside this flow region than is physically realistic; also, the assumed value of the shock-curvature term in (A 1*b*) used to produce these phase planes is likely to be too high for trajectories that penetrate fully into this region.

REFERENCES

Artem'eva, N. A. & Shuvalov, V. V. 1996 Interaction of shock waves during the passage of a disrupted meteoroid through the atmosphere. *Shock Waves* **5**, 359–367.

Artemieva, N. A. & Pierazzo, E. 2009 The Canyon Diablo impact event: projectile motion through the atmosphere. *Meteorit. Planet. Sci.* **44** (1), 25–42.

Artemieva, N. A. & Shuvalov, V. V. 2001 Motion of a fragmented meteoroid through the planetary atmosphere. *J. Geophys. Res.* **106** (E2), 3297–3309.

Barri, N. G. 2009 Aerodynamic interaction of meteor-body fragments: the collimation effect. *Dokl. Phys.* **54** (9), 423–425.

Berger, M. & Colella, P. 1988 Local adaptive mesh refinement for shock hydrodynamics. *J. Comput. Phys.* **82**, 64–84.

Bertin, J. J. & Cummings, R. M. 2006 Critical hypersonic aerothermodynamic phenomena. *Annu. Rev. Fluid Mech.* **38**, 129–157.

Billig, F. S. 1967 Shock-wave shapes around spherical- and cylindrical-nosed bodies. *J. Spacecr. Rockets* **4** (6), 822–823.

Bland, P. A. & Artemieva, N. A. 2003 Efficient disruption of small asteroids by Earth's atmosphere. *Nature* **424**, 288–291.

Bland, P. A. & Artemieva, N. A. 2006 The rate of small impacts on Earth. *Meteorit. Planet. Sci.* **41** (4), 607–631.

Chyba, C. F., Thomas, P. J. & Zahnle, K. J. 1993 The 1908 Tunguska explosion: atmospheric disruption of a stony asteroid. *Nature* **361**, 40–44.

Cirak, F., Deiterding, R. & Mauch, S. P. 2007 Large-scale fluid–structure interaction simulation of viscoplastic and fracturing thin shells subjected to shocks and detonations. *Comput. Struct.* **85** (11–14), 1049–1065.

Deiterding, R. 2003 Parallel adaptive simulation of multi-dimensional detonation structures. PhD thesis, Brandenburgische Technische Universität Cottbus.

Deiterding, R. 2005*a* Construction and application of an AMR algorithm for distributed memory computers. In *Adaptive Mesh Refinement: Theory and Applications* (ed. T. Plewa, T. Linde and V. G. Weirs), Lecture Notes in Computational Science and Engineering, vol. 41, pp. 361–372. Springer.

Deiterding, R. 2005*b* Detonation structure simulation with AMROC. In *High Performance Computing and Communications* (ed. L. T. Yang), Lecture Notes in Computer Science, vol. 3726, pp. 916–927. Springer.

Deiterding, R. 2009 A parallel adaptive method for simulating shock-induced combustion with detailed chemical kinetics in complex domains. *Comput. Struct.* **87**, 769–783.

Deiterding, R., Cirak, F. & Mauch, S. P. 2009 Efficient fluid–structure interaction simulation of viscoplastic and fracturing thin-shells subjected to underwater shock loading. In *Int. Workshop on Fluid–Structure Interaction* (ed. S. Hartmann, A. Meister, M. Schäfer and S. Turek), pp. 65–80. University Press GmbH.

Deiterding, R., Radovitzky, R., Mauch, S. P., Noels, L., Cummings, J. C. & Meiron, D. I. 2005 A virtual test facility for the efficient simulation of solid materials under high energy shock-wave loading. *Engng Comput.* **22** (3–4), 325–347.

Edney, B. E. 1968 Effects of shock impingement on the heat transfer around blunt bodies. *AIAA J.* **6** (1), 15–21.

Fedkiw, R. P., Aslam, T., Merriman, B. & Osher, S. 1999 A non-oscillatory Eulerian approach to interfaces in multimaterial flows (the ghost fluid method). *J. Comput. Phys.* **152**, 457–492.

Hayes, D. H. & Probstein, R. R. 1966 *Hypersonic Flow Theory*. Academic Press.

Heide, F. 1963 *Meteorites*. University of Chicago Press.

https://doi.org/10.1017/jfm.2011.57 Published online by Cambridge University Press

Hills, J. G. & Goda, M. P. 1993 The fragmentation of small asteroids in the atmosphere. *Astron. J.* **105** (3), 1114–1144.

Hoerner, S. F. 1965 *Fluid-Dynamic Drag: Practical Information on Aerodynamic Drag and Hydrodynamic Resistance*. Hoerner Fluid Dynamics.

Krinov, E. L. 1966 *Giant Meteorites, translated by J. S. Romankiewicz*. Pergamon Press.

Laurence, S. J. 2006 Proximal bodies in hypersonic flow. PhD thesis, California Institute of Technology, Pasadena, California.

Laurence, S. J., Deiterding, R. & Hornung, H. G. 2007 Proximal bodies in hypersonic flow. *J. Fluid Mech.* **590**, 209–237.

Lees, L. 1955 Hypersonic flow. In *Proc. 5th Intl Aero. Conf., Los Angeles*. Inst. Aero. Soc., pp. 241–276.

Passey, Q. R. & Melosh, H. J. 1980 Effects of atmospheric breakup on crater field formation. *Icarus* **42**, 211–233.

Sanderson, S. R., Hornung, H. G. & Sturtevant, B. 2004 The influence of non-equilibrium dissociation on the flow produced by shock impingement on a blunt body. *J. Fluid Mech.* **516**, 1–37.

Schultz, P. H. & Sugita, S. 1994 Penetrating and escaping the atmospheres of Venus and Earth. In *25th Lunar and Planetary Science Conference*, pp. 1215–1216.

Sedov, L. I. 1959 *Similarity and Dimensional Methods in Mechanics* (translation edited by Maurice Holt; translation by Morris Friedman from the fourth Russian edition). Academic Press.

Svetsov, V. V., Nemtchinov, I. V. & Teterev, A. V. 1995 Disintegration of large meteoroids in Earth's atmosphere: theoretical models. *Icarus* **116**, 131–153.

Toro, E. F. 1999 *Riemann Solvers and Numerical Methods for Fluid Dynamics*. Springer.

Vincenti, W. G. & Kruger, C. H. 1965 *Introduction to Physical Gas Dynamics*. Wiley.

https://doi.org/10.1017/jfm.2011.57 Published online by Cambridge University Press